communications materials

A Nature Portfolio journal

Article

https://doi.org/10.1038/s43246-025-01024-6

Unveiling the structure–magnetism interplay in the ferrimagnetic pyrochlore Gd_2CrSbO_7 with significant cryo–magnetocaloric performance

R. S. Silva Jr[1,2,3] ✉, **J. E. Rodrigues**[1,4], **C. Santos**[5], **Ch Sahle**[4], **F. Serrano-Sánchez**[1], **H. L. Andersen**[1], **J. Gainza**[1,4], **A. Skorynina**[6], **N. Biskup**[2,7], **N. M. Nemes**[1,2], **E. C. Passamani**[5], **J. L. Martínez**[1], **N. S. Ferreira**[3] & **J. A. Alonso**[1] ✉

Magnetic refrigeration is a promising and efficient cooling technology that uses the magnetocaloric effect (MCE), requiring particular materials with low heat capacity, low ordering temperature, and large magnetic moments for high performance. Here we report on Gd_2CrSbO_7, a mixed B-site pyrochlore oxide that exhibits a significant cryogenic MCE, driven by intricate 4*f*–3 *d* exchange interactions. Our combined experimental and theoretical investigation reveals that Gd_2CrSbO_7 crystallizes in a cubic pyrochlore structure ($Fd\bar{3}m$) with ferrimagnetic (FiM) ordering, uniquely hosting a Griffiths-like phase and a Schottky anomaly arising from competing Cr–Cr short-range interactions and Gd crystal field effects. X-ray Raman spectroscopy confirms super-exchange interactions, while EXAFS analysis identifies enhanced Sb–O bond rigidity, influencing the material's stability. Notably, Gd_2CrSbO_7 achieves a remarkable maximum magnetic entropy change of $-\Delta S_M^{max} \approx 21$ J/kg K and refrigerant capacity of $RC \approx 430$ J/kg (at 0 − 7 T), comparable to benchmark cryogenic refrigerants like $Gd_3Ga_5O_{12}$, but containing substantially low-priced elements. These findings position Gd_2CrSbO_7 as a promising platform for next-generation magnetic cooling, while shedding light on emergent magnetic and electronic phenomena in pyrochlore oxides.

The urgent need for energy-efficient and environmentally sustainable cooling technologies has propelled magnetic refrigeration (MR), based on the principle of the magnetocaloric effect (MCE), to the forefront of next-generation solid-state cooling solutions[1]. The MCE is an inherent magnetothermal response of magnetic solids to an external magnetic field, which originates from the interaction between the magnetic field and the material magnetic sublattice(s). Thus, it is strongly correlated with the properties of the structural and magnetic phase transitions (MPTs)[2,3]. High-performance magnetocaloric materials require some stringent thermodynamic features, including low lattice and electronic heat capacities to minimize internal heating, low ordering temperatures to enable efficient cryogenic operation, large magnetic moments, and high thermal conductivity[4]. As in the case of the benchmark refrigerant gadolinium-gallium garnet $Gd_3Ga_5O_{12}$ (GGG)[5,6], compounds in which only the Gd^{3+} spin is present become quite attractive due to the fact that Gd has a special electronic configuration with spherical charge distribution due to its half-filled 4 *f* shell ("S-state atom"), which leads to a large total moment J of 7/2 and quenched angular moment L = 0. The mentioned material with record-high MCE has as main drawback the elevated price of Ga element; consequently, a wide range of Gd-containing magnetic materials with earth-abundant elements and different structural features were systematically studied in the past decades, such as $NaGdS_2$[7], $LiGdF_4$[8], GdF_3[9], $\{Gd_{12}Na_6\}$-molecular quadruple-wheel[10], Gd-UiO-66[11], $GdPO_4$[12], Gd_2SiO_5[13], $Gd(HCOO)_3$[14], $Gd(OH)CO_3$[15], $Gd(OH)F_2$[16], $GdSrCoFeO_6$[17], and Sr_2GdSbO_6[18], to be promising refrigerant materials.

---

[1]Instituto de Ciencia de Materiales de Madrid (ICMM), CSIC, Madrid, Spain. [2]Departamento Física de Materiales, Universidad Complutense de Madrid, Madrid, Spain. [3]Departamento de Física, Universidade Federal de Sergipe, São Cristóvão, Sergipe, Brazil. [4]European Synchrotron Radiation Facility (ESRF), 71 Avenue des Martyrs, Grenoble, France. [5]Departamento de Física, Universidade Federal do Espírito Santo, Vitória, Espírito Santo, Brazil. [6]CELLS – ALBA Synchrotron Light Source, Barcelona, Spain. [7]Instituto Pluridisciplinar, Universidad Complutense de Madrid, Madrid, Spain. ✉e-mail: rsantoss@ucm.es; ja.alonso@icmm.csic.es

Particularly, the pyrochlore-type compounds with the general formula $A_2B_2O_7$ (where A^{3+} is a rare earth (RE) ion and B^{4+} a 3 *d*, 4 *d*, or 5 *d* transition metal ion)[19] have been extensively studied during decades, and are characterized by geometrically frustrated magnetic structures, where the A and B ions are located at two distinct interpenetrating lattices of corner-sharing tetrahedra. These materials exhibit fascinating low-temperature physical properties, including quantum spin-ice behavior, partial magnetic orders, competing magnetic orders, spin-glass-like features, and spin-fluid behavior[20,21]. Compounds, such as $R_2Mn_2O_7$ (R = Dy, Ho, Yb, Er)[22,23], $Dy_2Si_2O_7$[24], and $Y_2Ir_{2-x}Cr_xO_7$[25] with different combinations of elements in the pyrochlore structure, have their MCE properties investigated. Specifically, these systems exhibit a maximum magnetic entropy change ($-\Delta S_M^{max}$) with values at the interval 1.73–20.33 J/kg K (under an applied magnetic field change (ΔB_{ap}) of 0–7 T). Moreover, several other Gd-based pyrochlore oxides were recently reported to exhibit a large MCE at low temperatures. For instance, Zhang et al.[21] reported that the geometrically frustrated $Gd_2Ti_2O_7$, which exhibits an antiferromagnetic ground state, achieves a $-\Delta S_M^{max}$ of 28.69 J/kg K and refrigeration capacity (RC) of 240.67 J/kg at $T \approx 3$ K under an ΔB_{ap} of 0–7 T. In contrast, for the $Gd_2Si_2O_7$[24], a $-\Delta S_M^{max} \approx 58$ J/kg K at 3 K was reported, however, no long-range ordering was found at temperatures down to 2 K. Meanwhile, Koskelo et al.[26] obtained a $-\Delta S_M^{max} = 32$ mJ/kg K for the Heisenberg antiferromagnet $Gd_2Sn_2O_7$, which highlights the importance of the degree of magnetic frustration and lattice geometry in determining magnetocaloric performances. Despite several studies conducted, much remains to be done to optimize the MCE in these pyrochlore families, consequently a chemical substitution seems to be a promising approach to tune some desired magnetocaloric properties.

Concerning the canonical pyrochlore family, it can be expanded to include the mixed pyrochlores, $A_2(B'^{3+} + B''^{5+})O_7$, replacing half of the nonmagnetic transition metal ions at B-site, but imposing the charge neutrality criteria for the structurally ordered pyrochlores[27]. For instance, Nandi et al.[27] reported that mixed B-site pyrochlore Dy_2FeSbO_7 has a spin ice-like ground state at low temperatures with net ferromagnetic (FM) interactions between the pairs of Dy-Dy, Fe-Fe, and Dy-Fe. This leads to spin configurations, where the Ising-like Dy-spins are arranged in macroscopically disordered 'two-in, two-out' configurations in the tetrahedron. They also found a ΔS value at zero-field equal to the spin-ice value of 4.1 J/K mol at 11 K. Substituting Fe^{3+} ions by Cr^{3+}, Whitaker et al.[28]. previously investigated these compounds for several RE, such as RE_2CrSbO_7 (RE = Ho, Y, Tb, Dy, Er). Generally, these pyrochlores exhibit FM ordering due to the predominance of Cr–Cr interactions. In particular, the Ho_2CrSbO_7 forms an "ordered spin-ice structure" below 13 K, where the Ho^{3+} spins are constrained along the ⟨111⟩ axes. On the other hand, Cr^{3+} ions interact magnetically through Cr^{3+}-O-Cr^{3+} chains with 130° bonds throughout the structure, and therefore, are considered crucial for inducing Ho^{3+} magnetic ordering at low temperatures. Surprisingly, only a few articles focused on the magnetocaloric properties of the Gd^{3+}-based mixed B-site pyrochlores. Recently, Nandi et al.[29] extensively investigated the magneto-thermodynamic properties of the pyrochlore Gd_2FeSbO_7. This compound exhibits a complex magnetic structure characterized by intra-sublattice Gd–Gd antiferromagnetic (AFM) interactions, intra-sublattice Fe–Fe FM interactions, and other inter-sublattice Gd–Fe interactions, which is AFM in nature. The $3d^5$ Fe^{3+} exchange interactions, which are stronger than the $4f^7$ Gd interactions, generate a molecular field at the Gd-site through the weaker cooperative Gd–Fe (4*f*–3*d*) interactions. Additionally, the spin frustration index $f \approx 2.5$ indicates that this system is moderately frustrated, potentially preventing the formation of the Palmer-Chalker ground state configuration in the Gd sublattice at lower temperatures. These unique features provide a new avenue for exploring the intriguing magnetism behavior in such pyrochlore systems.

In this study, we present a systematic experimental and theoretical investigation into mixed B-site pyrochlore Gd_2CrSbO_7, containing earth-abundant and inexpensive elements, regarding its structural, electronic, and magnetic properties, and especially its MCE performance. Gd_2CrSbO_7 crystallizes in the cubic pyrochlore structure with space group $Fd\bar{3}m$, such that Cr/Sb octahedra form a corner-sharing lattice, while the eight-fold coordinated Gd polyhedra are edge-sharing with both the neighboring Cr/Sb octahedra and other Gd polyhedra. The magnetic ground state has been verified in detail as a ferrimagnetic coupling from 4*f*–3*d* exchange magnetic interactions by magnetization measurements and first-principles calculations. Interestingly, the existence of a Griffiths-like phase and a Schottky anomaly is also observed, which are related to the competition between short-range magnetic interactions. Most significantly, the substantial magnetocaloric performance, associated with their high values of $-\Delta S_M^{max}$ and RC, is comparable with several state-of-the-art magnetocaloric materials, consequently making the Gd_2CrSbO_7 compound a promising solid refrigerant for low-temperature magnetic cooling technology.

Results

Crystalline structure at room temperature

Figure 1a shows the Rietveld refinement of the total scattering (TS) data at room temperature (RT), confirming that the Gd_2CrSbO_7 sample crystallizes in a cubic pyrochlore structure with space group $Fd\bar{3}m$, with a refined lattice parameter of $a = 10.26183(2)$ Å. No additional crystalline phases were identified, indicating the sample is a single-phase material. Detailed results of the Rietveld refinement are provided in Supplementary Table 1. As illustrated in the 3D structure view depicted in Fig. 1b and d, the Cr^{3+} and Sb^{5+} cations are distributed at random at 16*d* (½,½,½) sites forming distorted octahedra with O2 oxygen atoms at 48*f* (*x*,1/8,1/8) sites. The Gd^{3+} ions are located at 16*c* (0,0,0) sites in distorted cube coordination with two kinds of non-equivalent oxygen ions (O1 and O2) at 8*b* (1/8,1/8,1/8) and 48*f* (*x*,1/8,1/8) sites, respectively. The Cr/Sb octahedra form a corner-sharing lattice, whereas the Gd polyhedra are edge-sharing with both the neighboring Cr/Sb octahedra, as well as other Gd polyhedra.

To examine the local structure of Gd_2CrSbO_7, we performed X-ray atomic pair distribution function (PDF) analysis of the room temperature TS data. Here, an experimental background (capillary and air scattering) was collected on an empty capillary and subtracted from the data to isolate the sample scattering contribution. The obtained PDF was fitted in real space in the 1–30 Å range using the same model as the reciprocal space Rietveld analysis. It yields a very good agreement with the data ($R_w = 8.23\%$), as represented in Fig. 1c. The PDF analysis does not indicate any local structural deviations, e.g., interstitial or local ordering of Cr and Sb in the mixed metal Cr/Sb site, from the average long-range structure obtained from the Rietveld analysis. Notably, the PDF is dominated by the characteristic metal-metal distances due to their higher scattering power compared to oxygen, as well as the relatively high multiplicity of the metal-metal atomic pairs in the structure (see Fig. 1d and Supplementary Table 2). For instance, the first major peak at 3.628 Å (black arrow in Fig. 1c) arises due to the combined nearest neighbor metal-metal distances in the structure, i.e. Cr/Sb-Cr/Sb, Gd-Cr/Sb, and Gd-Gd correlations, which occur 384 times per unit cell, thus presenting a much higher signal than the closer metal-oxygen and oxygen-oxygen distances.

Scanning Transmission Electron Microscopy analysis

Atomic resolution imaging and spectroscopy were performed on three different grains along the [001], [111], and [011] zone axes. Here, we present the results from the grain oriented along the [001] zone axis due to its relatively lower spatial drift compared to the other directions. In Fig. 2a displays the inverse annular bright field (ABF) image of this crystallite. The inverse ABF image resembles an annular dark field (ADF) image (see in Fig. 2c) but allows for enhanced detection of lighter elements, such as oxygen. The bright spots visible in Fig. 2a, c represent Gd and Cr/Sb atoms, which are indistinguishable when projected along the [001] zone axis. The weak spots located at the centers of alternating squares in Fig. 2a correspond to four closely positioned oxygen atoms, as indicated by the embedded crystal cell determined through Rietveld refinement. The electron energy

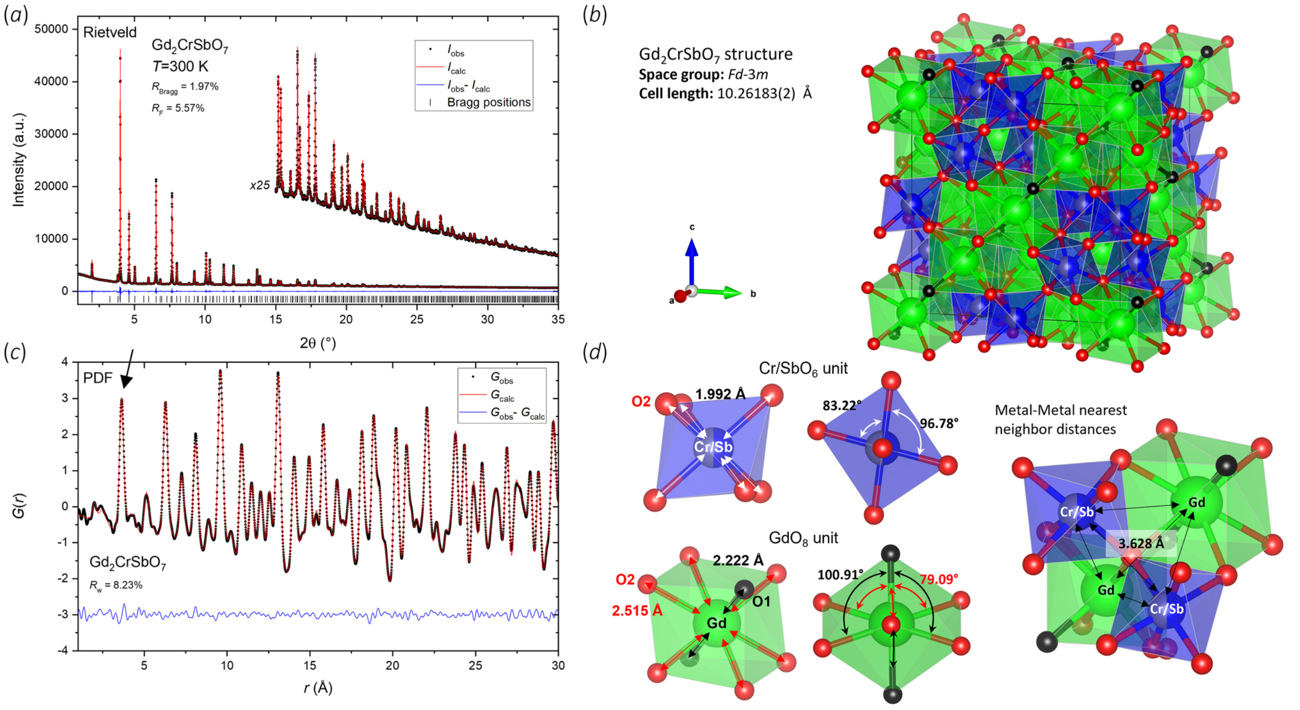

Fig. 1 | Crystalline structure characterization at room temperature. a Room temperature total scattering data of the Gd_2CrSbO_7 sample and corresponding Rietveld fit. **b** Illustration of the Gd_2CrSbO_7 crystal structure. The green polyhedra/spheres indicate the Gd position, blue/(gray) polyhedra/spheres indicate the Cr/(Sb) position, and the black and red spheres correspond to the O1 and O2 oxygen ions, respectively. **c** Room temperature X-ray PDF data and corresponding fit. **d** Illustration of the local structural units and nearest neighbor metal-metal distances in the crystalline structure. The structural illustrations were made using the software VESTA[72].

loss spectrum (EELS) data is represented in Fig. 2b, displaying the oxygen *K*, chromium $L_{2,3}$, antimony $M_{4,5}$, and gadolinium $M_{4,5}$ edges. The corresponding elemental maps are shown in Fig. 2c, alongside the survey image of the analyzed region and the simultaneous ADF image obtained during EELS acquisition. The elemental mapping confirms that bright spots correspond to heavy elements, Gd at the A site and Cr/Sb at the B-site. The homogeneous distribution of Cr and Sb demonstrates their disordered arrangement on the B-site. Oxygen atoms in this $A_2B_2O_7$ pyrochlore structure occupy the interstitial spaces between the heavy atoms, stabilizing the crystal framework.

Magnetoelastic effect and thermal expansion

The magnetoelastic effect in Gd_2CrSbO_7 was investigated from temperature-dependent SXRD patterns collected in the temperature range 10–400 K. The raw SXRD data are presented in Fig. 3a, while its inset details the evolution of the main Bragg reflection (222). No additional peaks were detected in the entire temperature interval, thus ruling out any global structural transition down to 10 K (see Fig. 3b). Detailed results of the Rietveld refinement from SXRD data at 10–400 K range are provided in Supplementary Fig. 1 and Supplementary Table 3. A significant thermal contraction was observed from 400 K down to 60 K; below this temperature there is no further contraction (see Fig. 3c and Supplementary Fig. 2). The total volumetric coefficient of thermal expansion $\alpha_V = \Delta V/V_i\Delta T$ [30] (V_i is the initial volume and ΔV is the volume change corresponding to the temperature change ΔT) of 1.51×10^{-5} K^{-1} (+0.58%). We treated the volume expansion using the Grüneisen approximation to the zero-pressure equation of state according to its first-order expansion[31] (see description in Supplementary Information), yielding $V_0 = 1076.75(7)$ Å^3, $\theta_D = 415.7$ K, and $\gamma/B_0 = 6.497 \times 10^{-12}$ Pa^{-1} (the parameters are: V_0 unit-cell volume at 0 K, B_0 the isothermal bulk modulus, and γ the Grüneisen coefficient).

It is worth addressing the subtle splitting observed in Fig. 3a at intermediate temperatures (30–150 K), absent at 10 K and above 200 K, that likely arises from magnetoelastic coupling in this intrinsically disordered system. The random Cr^{3+}/Sb^{5+} ions occupancy at the same Wyckoff sites (16*d* in the $Fd\bar{3}m$ space group) and inherent geometric frustration may induce complex local distortions. In a comparable pyrochlore system, $Tb_2Ti_2O_7$[32], the high-resolution single-crystal XRD revealed cubic-to-tetragonal fluctuations below 20 K, manifested by Bragg peak broadening and anomalous unit-cell expansion. Nevertheless, the cubic pyrochlore model ($Fd\bar{3}m$) proved robust in describing our system, successfully refining the data across the entire temperature range and producing consistently low R_{Bragg} factors between 2 and 3% (see Supplementary Table 3). Moreover, Pawley fittings in tetragonal space groups ($I\text{-}4m2$, $I4_1/amd$, $I4_122$, etc.) proved unsuccessful, producing identical results to the cubic $Fd\bar{3}m$ model. The corresponding Rietveld plots (Supplementary Fig. 1) demonstrate satisfactory fits across all temperatures. To further clarify the local crystal structure of Gd_2CrSbO_7 at low temperatures, we carried out PDF analysis of synchrotron TS data collected at 30 and 150 K. At both temperatures, the local structure could be accurately modeled using the cubic $Fd\bar{3}m$ structure (see Supplementary Fig. 3), yielding an excellent fit to the experimental data, which is consistent with our SXRD results indicating a cubic structure across the 10–400 K temperature range. Although the unit-cell volume in Fig. 3c appears unchanged between 10–60 K, a detailed analysis of the local crystal structure based on the average Gd–O and Cr/Sb–O bond lengths, as well as average Gd–O2–Gd and Cr/Sb–O1–Cr/Sb bond angles (see Supplementary Fig. 4) exhibit anomalies followed by a slope change in the vicinity of the magnetic transition temperature T_C (discussed later). We infer that the underlying thermal contraction stabilizes the magnetic behavior of Gd_2CrSbO_7 at temperatures below 100 K, which can be attributed to a magnetoelastic coupling similar to that reported for $Tb_2Ti_2O_7$[32].

To expand the analysis, the individual atomic oscillations was accessed using the mean square displacements (MSDs or U_{iso} in units of Å^2)[33]. The experimental U_{iso} values for O (O1 and O2), Gd, and Cr/Sb sites, extracted from the Rietveld refinement, are shown in Fig. 3d, e. The U_{iso} for oxygen sites decrease regularly from 400 K down to 250 K, as expected, but exhibit an anomalous behavior in the range 25–225 K, which can be related to the

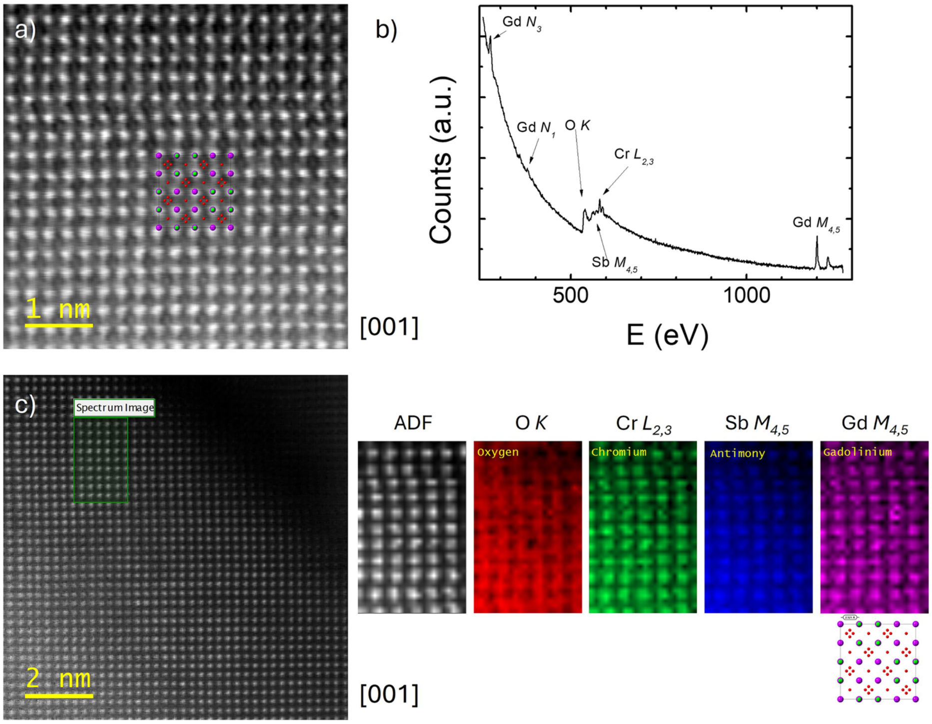

Fig. 2 | Microstructural and elemental investigation from STEM and EELS. **a** Inverse ABF image of the Gd_2CrSbO_7 crystal along the [001] zone axis. **b** The EELS spectrum. **c** EELS elemental mapping: from the left, the survey image of the region where EELS is taken, simultaneous ADF image during the EELS acquisition, and elemental maps based on O K, Cr $L_{2,3}$, Sb $M_{4,5}$, and Gd $M_{4,5}$ edges.

possible magnetoelastic effects in Gd_2CrSbO_7 pyrochlore. However, the U_{iso} for Gd and Cr/Sb could be fitted by the Debye model for the individual atomic oscillations, as described by Eq. S2 (see in Supplementary Information). The obtained fit provides the intrinsic disorder at 0 K and the Debye temperature (θ_D). In this sense, the derived intrinsic disorder from the best fit was 8.8×10^{-3} Å^2 and 1.4×10^{-3} Å^2 for Gd and Cr/Sb, respectively, and the Debye temperatures were obtained as 291.7 K (Gd) and 514.9 K (Cr/Sb). Those values can be used to estimate the bonding stiffness considering the harmonic one-particle potential (OPP)[34], by applying the following expression:

$$K_D = \frac{mk_B^2\theta_D^2}{3\hbar^2} \tag{1}$$

where K_D is the force constant (in units of eV/Å^2), which provided values of 7.9 and 13.6 eV/Å^2 for the (Gd), and (Cr/Sb) sites, respectively. Such values increase in the order $K_{(\mathrm{Gd})} < K_{(\mathrm{Cr/Sb})}$, meaning that the distorted octahedral units of Cr and Sb are more constrained to their motions (indeed, with $d_s^2 = 1.4 \times 10^{-3}$ Å^2). This conclusion essentially is because the (Cr/Sb)–O bond is more rigid when compared to (Gd)–O, which has an intrinsic disorder ~6 times higher than that of the (Cr/Sb) site.

Extended X-ray absorption spectroscopy

In Fig. 4a, the raw Sb K-edge EXAFS spectrum of Gd_2CrSbO_7 at 100 K is shown (dot symbols) together with the fitting composed of individual oscillations (total of four, being plotted as grey lines). The composed sum of these oscillations constitutes the best-fit EXAFS signal (red line). In Fig. 4b, the corresponding Fourier transform is represented. To fit the EXAFS oscillations, four single scattering (SS) paths were considered as a reliable approximation of the local atomic structure surrounding the Sb atoms. In particular, the atomic paths encompass the Sb–O [fixed coordination number (CN) to 6] bond and the single scattering paths Sb–Gd ($CN = 6$), Sb–Sb ($CN = 3$), and Sb–Cr ($CN = 3$). The parameters extracted from the EXAFS fit analysis at 100 K are summarized in Supplementary Table 4. The statistical agreement and fit quality assessed the reliability of our structural model to describe the local structure around Sb atoms in the Cd_2CrSbO_7 pyrochlore.

The structural stability of Gd_2CrSbO_7 was also probed using temperature-dependent EXAFS data in the range 100—500 K. The previous model exhibited high stability during the entire temperature range, as demonstrated by the almost constant variation of the R-factor between 0.0054 (at 100 K) and 0.0112 (at 500 K). The temperature-dependent $k^3\chi(k)$ oscillations are represented in Fig. 4c, showing no evidence of temperature-induced phase transitions. On the other hand, the evolution of the local parameters with temperature can provide valuable information on the lattice dynamics and stability from the point of view of the antimony atoms. Particularly, we have investigated the behavior of the Debye-Waller factor (σ^2) for two most intense scattering paths Sb–O and Sb–Gd using the Einstein formalism[35,36], being defined as follows:

$$\sigma^2(T) = \sigma_0^2 + \frac{\hbar^2}{2\mu k_B\theta_E}\coth\left(\frac{\theta_E}{2T}\right), \tag{2}$$

where θ_E is the Einstein temperature, σ_0 the static disorder, and μ the reduced mass of the scattering path under evaluation (Sb–O or Sb–Gd). From the best fit of σ^2 using the Einstein formalism, we have obtained the Einstein temperatures of 757 K and 211 K for the scattering paths Sb–O and Sb–Gd, respectively, as shown in Fig. 4d and e. The fitted Einstein temperatures provide an estimate of the force constant (κ_E) for the paths using the harmonic approximation of the atomic potential ($\kappa_E = \frac{\mu k_B^2\theta_E^2}{\hbar^2}$)[37]. The derived force constants are quite different $\kappa_{E(Sb-O)} \gg \kappa_{E(Sb-Gd)}$, in particular $\kappa_{E(Sb-O)}$ ~ 14.4 eV·Å^{-1} and $\kappa_{E(Sb-Gd)}$ ~ 2.9 eV·Å^{-1}. This result suggests that the atomic interactions with oxygen are more rigid and more covalent compared to the gadolinium sublattice.

X-ray Raman scattering

We conducted X-ray Raman scattering (XRS) experiments at Cr $L_{2,3}$, Gd $N_{4,5}$, and O K edge to explore the electronic structure and possible super-exchange interactions in the Gd_2CrSbO_7 pyrochlore. The XRS spectrum of the Cr $L_{2,3}$-edge is shown in Fig. 5a. Since the momentum transfer dependence is negligible in this case, we averaged over signals of medium- and high momentum transfer regions ($q = 6.35$ and 8.61 Å^{-1}, respectively). We used multiplet simulations, including charge-transfer and ligand field effects

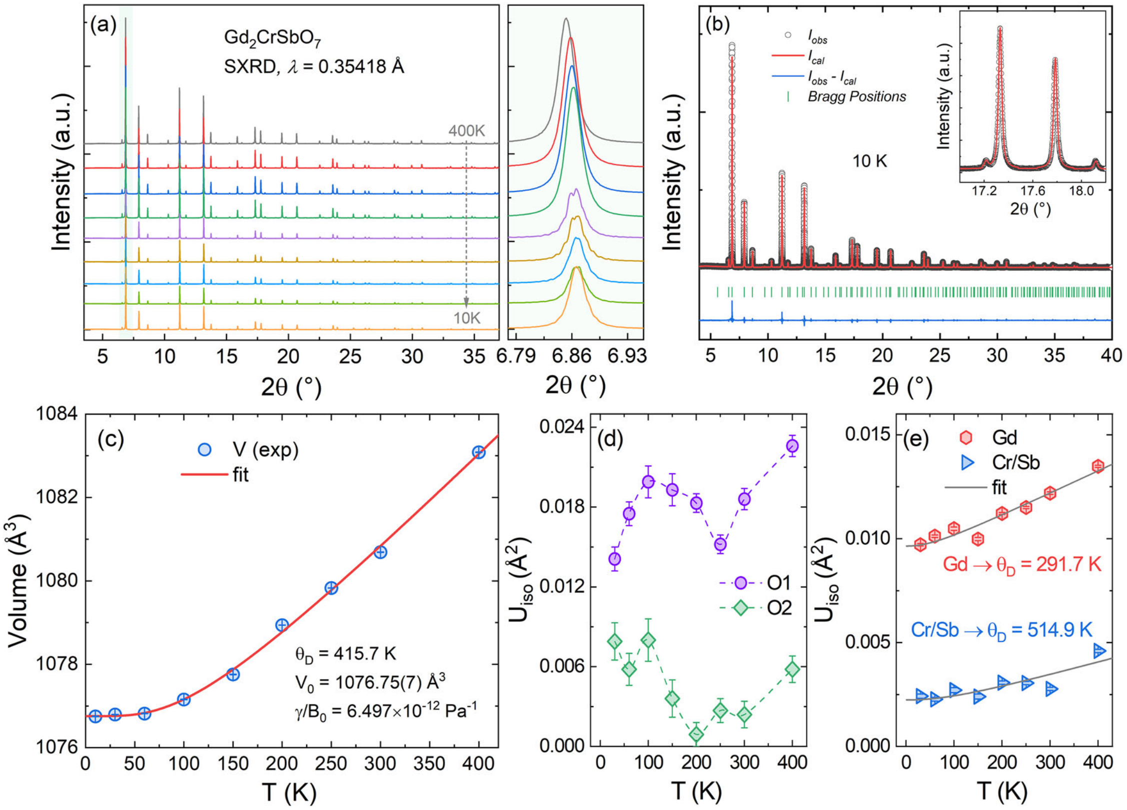

Fig. 3 | Magnetoelastic effect investigation from temperature-dependent SXRD data. **a** Temperature evolution in the temperature range 10–400 K; inset shows the evolution of the Bragg reflection (222). **b** Rietveld refinement of the synchrotron X-ray diffraction pattern of the Gd_2CrSbO_7 pyrochlore; inset elucidates the quality of the refinement for intermediate 2θ angles. **c** Thermal expansion of the unit cell (circles) and the red line represents the fitting result using the Grüneisen approximation. **d**, **e** Temperature dependence of the mean-square displacements U_{iso} for the O (O1 and O2), Gd, and Cr/Sb sites.

(LFMT) as implemented in the Hilbert^{++} code[38,39], to fit the spectrum. Since Hilbert^{++} allows arbitrary symmetry of the ligands, we used the oxygen positions refined by XRD to define the ligand field around the Cr ions. The overall shape of the experimental data is reasonably reproduced by a model based on Cr ions with electronic configuration $3d^3$ in a pseudo-octahedral crystal field. Under this condition, it splits the levels by approximately 10Dq = 2 eV. The one-electron energy diagram of the initial state is shown in Fig. 5a as inset. We used a screening factor for the Slater integrals of 0.65, i.e., at the lower end of the spectrum of reduction factors used for the calculation of the *L*-edges of the *3d* transition metals. This possibly points toward significant screening effects, including orbital ones that are not explicitly considered in our LFMT model, which encompassed only Cr *3d* and ligand *2p* orbitals. These effects may be related to the proposed superexchange interactions mentioned earlier.

XRS spectra of the $N_{4,5}$-edge of Gd in Gd_2CrSbO_7 are shown in Fig. 5b for different momentum transfers. As for the $N_{4,5}$ edge spectra of other lanthanides[40,41], the N_{45}-edge of Gd exhibits a strong momentum transfer dependence with a broad giant dipole resonance at low momentum transfer (light blue) centered at energy losses around 150 eV and sharp multiplet peaks at higher momentum transfer (dark blue) at lower energy losses. Due to the localized nature of the 4*f* orbitals in Gd, these spectra are less sensitive to the inter-atomic interactions, but they are true fingerprints of the 4*f* filling[42]. LFMT spectra for the different momentum transfers are shown as thin grey lines in Fig. 5b. The experimental spectra are well reproduced with a Gd^{3+} ($4f^7$, $5d^0$, $6s^0$) configuration. We used an arctan function with an onset at 158 eV energy loss to represent the continuum states not included in the multiplet model. At low momentum transfer, we convoluted the sharp atomic resonances with a Fano line shape to mimic the interaction between the higher energy dipole that allowed multiplet states with the continuum ones[43].

The O *K*-edge spectrum is shown in Fig. 5c together with results of spectrum simulations based on the full-multiple scattering approach implemented in *FDMNES*[44]. As for the Cr $L_{2,3}$-edge, the presented experimental spectrum (solid blue line) is an average over the medium- and high momentum transfer data, justified by the small momentum transfer dependence. Several broad features are visible centered around 533, 536, and 542.5 eV energy loss. These features are well-described by the spectrum calculations (thin black and gray solid lines), which are based on the atomic structures as described above. Spectral weight between 537.5 and 540.5 eV energy loss, however, is underestimated by the theory. The three spectrum calculations differ in the degree of core-hole screening, where the intensity of the first peak at 533 eV energy loss gains spectral weight with decreasing effect of screening. Projected density of states calculations showed that this peak originates predominantly from mixing of oxygen *2p* (red dashed) and Gd *5d* (orange dashed-dotted) orbitals, implying significant charge sharing between O and Gd.

Magnetic Properties

The temperature-dependent magnetic susceptibility (χ) recorded under the external magnetic field (μ_0H_{dc}) of 0.01 T in the 1.8–300 K temperature range by both zero-field cooling (ZFC) and field cooling (FC) modes is displayed in Fig. 6a. In fact, there is no significant irreversibility between ZFC and FC curves in almost the entire measured temperature range, except below ~20 K, exhibiting a typical FM/FiM (ferrimagnetic) order behavior with a transition to paramagnetic (PM) state at room temperature (as can be seen in the isothermal M(μ_0H) curves in Fig. 6b). From the first derivative of M_{FC} curve (see in Supplementary Fig. 5a), we estimated the $T_{Gd} \approx 12$ K (temperature at which the Gd^{3+} moment contributes more to the total susceptibility) and $T_C \approx 70$ K (magnetic transition temperature from FM/FiM to PM).

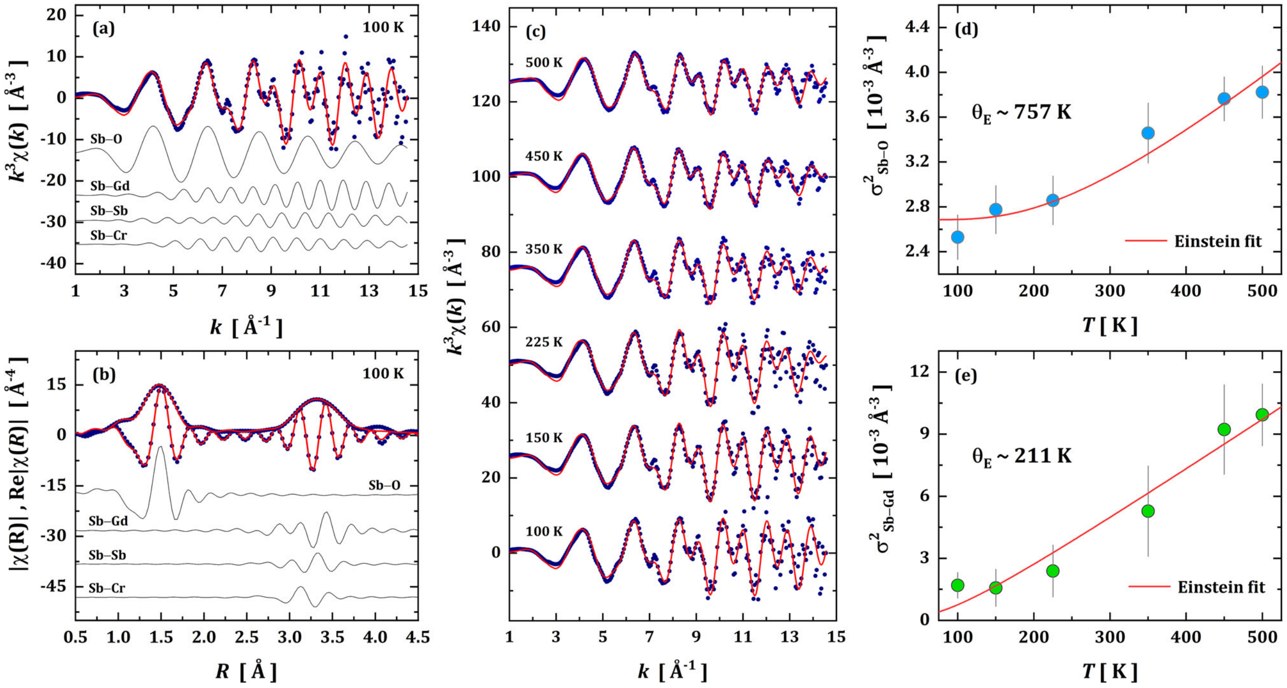

Fig. 4 | Temperature-dependent EXAFS analysis. Raw Sb *K*-edge EXAFS function χ(*k*) at 100 K (**a**) and its Fourier transform magnitude |χ(*R*)| and the real part Re[χ(*R*)] (**b**). The black lines represent individual fitted single scattering paths, while dot symbols depict the experimental points, and the red solid lines illustrate the fitted summed EXAFS signal (**c**). Temperature dependence of the Debye–Waller factor for Sb−O (**d**) and Sb−Gd (**e**); vertical bars represent the estimated error from EXAFS fitting for σ^2 parameter. In **d**, **e**, the red lines represent the best fit to the Einstein model (Einstein temperatures θ_E are also shown).

To further verify the magnetic transition temperatures, we perform frequency-dependent (0.1–1000 Hz) *ac* magnetic susceptibility (χ') measurements and specific heat (C_p) measurements at different applied fields (0.5–9.0 T), as shown in Fig. 6c, d, respectively. The χ'(T) curves are independent of frequency with decreasing temperature down to T_C, whereas below T_C, we observe a strong frequency- and field-dependence (see in Supplementary Fig. 5b, c), which becomes more evident in the prominent peak around 5 K (see inset of Fig. 6c). Similarly, C_p/T(T) plots exhibited a significant peak at low temperature at $T_{peak} \approx 2.3$ K, which becomes broad and displaced to higher temperatures as the applied field increases (see in Fig. 6d). Thus, this observation indicates a lack of long-range ordering in the spin structure at lower temperatures. Indeed, this behavior can be associated with the Schottky anomaly at low temperatures that arises from crystal field transitions related mostly to the *f*-electrons of Gd^{3+} [17]. The Schottky model explains this phenomenon through statistical physics by considering a few-level system with thermal occupation by:

$$C_{Sch}(T) = \left[\frac{\sum \nu_i \Delta_i^2 e^{-\Delta_i/T}}{\sum \nu_i e^{-\Delta_i/T}} - \left(\frac{\sum \nu_i \Delta_i e^{-\Delta_i/T}}{\sum \nu_i e^{-\Delta_i/T}}\right)^2\right] \qquad (3)$$

Where Δ_i are the energy gaps (in K units), $\Delta_0 = 0$ corresponds to the ground level, while the number and degeneracy of levels ν_i are fixed, leaving only one fitting parameter for 2-level systems. Herein, the Schottky anomaly was well-modeled using a doubly degenerate ground state and a non-degenerate excited state (see fits in Fig. 6 d), as other degeneracy choices yielded significantly poorer fits. The extracted level splitting varied linearly with the magnetic field (0–9 T) between 7.4–17 K, as displayed in the inset of Fig. 6d. This confirms that the low-temperature heat capacity peak, attributed to the Schottky anomaly, originates from crystal field effects in the Gd ions.

The inverse susceptibility plot was fitted in the PM temperature range with the Curie–Weiss (CW) equation $\chi = C/(T - \theta_{CW})$ [17] (inset of Fig. 6a), giving a FM-like $\theta_{CW} = 23$ K with local moment of 10.76 μ_B/f.u. This value aligns with the expected considering two Gd^{3+} (J = 7/2, gJ = 2, μ = 14.0 μ_B) and the Cr^{3+} sublattice ($3d^5$, S = 3/2, μ = 3.87 μ_B), with a theoretical value of $\mu_{theo} = 11.87$ μ_B/f.u. At 1.8 K, a saturation magnetic moment of ~16.8 μ_B/f.u. is observed in the M($\mu_0 H$) isotherm (see Fig. 6b), due to a total FM spin orientation, implying a parallel coupling of two Gd^{3+} and one Cr^{3+} magnetic moments, discussed later in the DFT section. In this case, unlike the B-site non-magnetic pyrochlores, i.e., $Gd_2B_2O_7$ (B = Ti, Sn, Pt, Ge)[45,46], the Gd_2CrSbO_7 system has a complex magnetic structure due to the magnetic Cr^{3+} ions on B-site, which provides additional Gd−O−Cr−O−Gd super-exchange interactions between two sublattices. Despite the identical Gd–Gd and Cr/Sb–Cr/Sb distances, the Cr/Sb–O distance is smaller compared to Gd–O one, as depicted in Fig. 1d, leading to weak Gd–Gd nearest-neighbor Heisenberg interactions. Instead, the interaction between the nearest-neighbor Cr ions tends to align the spins ferromagnetically[47], resulting in a positive θ_{CW} with FiM-like ordering, different from similar pyrochlore Gd_2FeSbO_7 with $\theta_{CW} < 0$[29], with effective AFM interactions. Also, the fact that $\theta_{CW} < T_C$ suggests the presence of clusters with short-range interactions in this temperature range, an assumption that can be supported by the high magnetic moment value of 16.83 μ_B discussed above.

Above T_C, a Griffiths-like phase was observed (downward curvature deviation from the CW fit in the inset of Fig. 6a) with a GP temperature of $T_{GP} \approx 125$ K, which is due to competition between short-range magnetic interactions correlation within the PM matrix. First, we fitted this region with the following power law relation $\chi^{-1} \approx \left(T - T_C^R\right)^{1-\lambda}$ (T_C^R is the critical temperature below, which χ diverges, and λ is an exponent such that $0 < \lambda < 1$ for $T_C^R < T < T_{GP}$ and $\lambda = 0$ for $T > T_{GP}$)[48]. The fit yields $T_C^R = 84.5 \pm 0.4$ K and $\lambda = 0.73 \pm 0.02$, which confirms the GP in Gd_2CrSbO_7. Second, the $\chi^{-1} \approx T/(T_C - 1)$ curve, plotted in the $log_{10}-log_{10}$ scale, was linearly fitted in both the FiM/FM and PM regimes to find out their λ values, respectively (see in Fig. 6e). The slope gives a $\lambda_{GP} = 0.956 \pm 0.004$ at temperature interval $T_C < T < 125$ K and $\lambda_{PM} = 0.137 \pm 0.002$ for $T > 125$ K, in the GP and PM state regimes, respectively; with an evident singularity region at $T_C < T < T_{GP}$. We attribute the observed GP due to the competing FM/AFM interactions, which are mediated by Gd−O−Cr−O−Gd super-exchange pathways and persist above T_C. These frustrated spin correlations stabilize the GP, which is consistent with phase competition in rare-earth pyrochlores such as

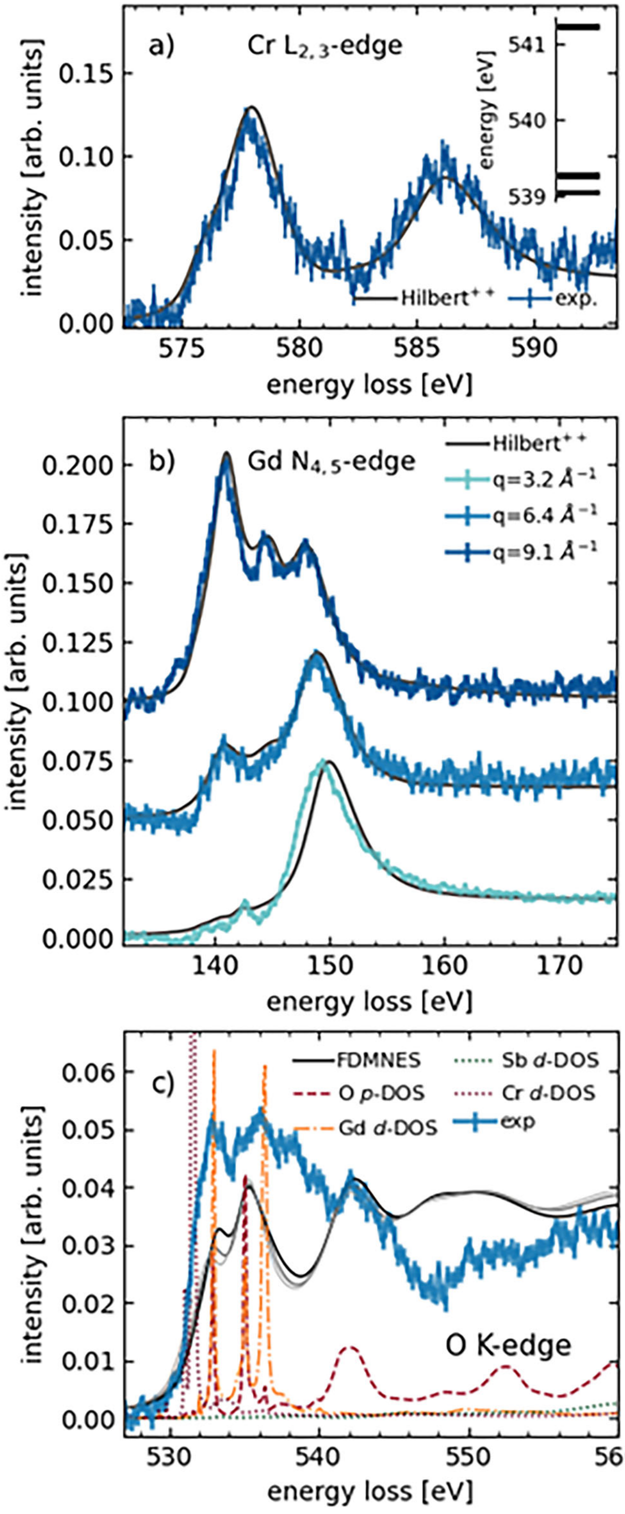

Fig. 5 | Experimental and simulated X-ray Raman scattering results. X-ray Raman spectra at room temperature for the Gd_2CrSbO_7 pyrochlore at **a** Cr L_{23}-, **b** Gd N_{45}-, and **c** O K-edges. Experimental data are represented as blue lines (low-, med-, and high-q) and simulated spectra are shown as black lines (using Hilbert^{++} or *FDMNES* codes). The dashed, dotted, and dashed-dotted lines represent the projected DOS calculations for Gd, Cr, Sb, and O.

$Ce_2Sn_2O_7$[49]. Crucially, the absence of frequency- and field-dependent spin glass signatures in our *ac* susceptibility data (see Fig. 6c and Supplementary Fig. 5b, c) supports this interpretation. Furthermore, as illustrated in Fig. 6f, the GP is progressively suppressed under applied fields up to 7 T, which is due to the masking of the FM/FiM signal by the rising PM background. These results further our understanding of GP in 3*d*–4*f* systems, highlighting their tunability through B-site chemical engineering, offering a means of controlling magnetic frustration in pyrochlores.

DFT studies

To further elucidate the magnetic and electronic ground-state properties of the Gd_2CrSbO_7 pyrochlore, spin-polarized DFT calculations were conducted. The stability of spin ordering was evaluated by simulating several magnetic cells with distinct spin orientations, as illustrated in Supplementary Fig. 6. Each magnetic cell, consisting of 22 atoms, was constructed using experimentally derived lattice parameters and atomic positions obtained from the SXRD data recorded at 10 K. The concentration of Cr/Sb dual-occupancy sites was kept constant, while their atomic positions were interchanged to reflect different chemical environments. Because Cr and Sb randomly occupy the same Wyckoff position, we modeled the B-sublattice as disordered. We replaced pair-specific couplings by effective exchanges J_{nB} and J'_{nB} for Gd–B pairs, obtained by configurational averaging over local B environments. As a result, the exchange network seems to be largely insensitive to the specific local arrangement of Cr and Sb, being the exchanges J_{nB} and J'_{nB} for Gd–B pairs (obtained by configurational averaging), while J_{nn} and J'_{nn} are considered for Cr–Cr. We sampled representative Cr/Sb arrangements within the supercell and verified that FiM4, the electronic densities of states (DOS) features, and local moments are robust across configurations (see details in Supplementary Section 5). The histogram of the simulated spin configurations as a function of their corresponding ground-state relative energies is displayed in Supplementary Fig. 7. The configurations with the lowest relative energies correspond to the FiM4, where these magnetic alignments, along with their DOS are shown in Fig. 7a, b. The calculations were initialized by optimizing the lattice structural parameters and internal forces. The results reveal that Gd spins exhibit predominantly FM coupling in the FiM4 state, resulting in longer bond lengths and a slight expansion of the unit cell due to the enhanced parallel alignment of magnetic moments.

The total (TDOS) and projected spin-polarized density of states (PDOS) (in Fig. 7a) provide insights into the electronic and magnetic properties of Gd_2CrSbO_7. The calculated average local magnetic moments on Gd (~7.0 μ_B) and Cr (~2.6 μ_B) ions are consistent across FiM4 configuration, indicating a stable magnetic contribution from these elements. An in-depth examination of orbital contributions to the energy bands reveals that the Sb^{5+} *s*- and *p*-states are not depicted in the PDOS due to their minimal overlap with the Fermi level, resulting in negligible contributions to the electronic and magnetic properties near the Fermi level. Similarly, the Sb^{5+} *d*-states, which are located in the deep valence region near −30 eV, have limited relevance to the material magnetic behavior and are, therefore, excluded from the detailed analysis. The Gd and Cr ions stabilize in 3+ charge state, as confirmed by the well-localized nature of the Gd 4*f* bands, which align with their substantial magnetic moments. Notably, the FiM4 configuration exhibits a high magnetic moment (μ_B/cell) due to the alignment of three Gd ions parallel to the Cr FM sublattice and one Gd ion antiparallel to it (as illustrated in Fig. 7b). This arrangement results in a net moment determined by the imbalance between the spin-up and spin-down DOS around −6.0 eV. Specifically, the broader Gd spin-up band relative to the spin-down band reflects a stronger FM-like interaction, leading to a larger total magnetic moment for the FiM4 configuration. Simultaneously, the exchange splitting between majority and minority spin bands near the Fermi level highlights the FM coupling at the Cr^{3+} sublattice. Further analysis of the electronic structure identifies Gd_2CrSbO_7 as a wide-bandgap semiconductor. As antiparallel magnetic interactions intensify, the tendency toward insulating behavior increases, resulting in a bandgap of 1.76 eV. Additional tests revealed that the calculated bandgap is sensitive to the Hubbard-U values applied to Cr. Nevertheless, the tendency toward an insulating electronic structure remains robust across a range of U values, indicating the stability of the insulating state. Moreover, the top of the valence band and the bottom of the conduction band are predominantly composed of Cr *3d* states hybridized with O *2p* orbitals, while the unoccupied Gd 5*d* bands are located mainly above 6.0 eV in the FiM4 configuration. The

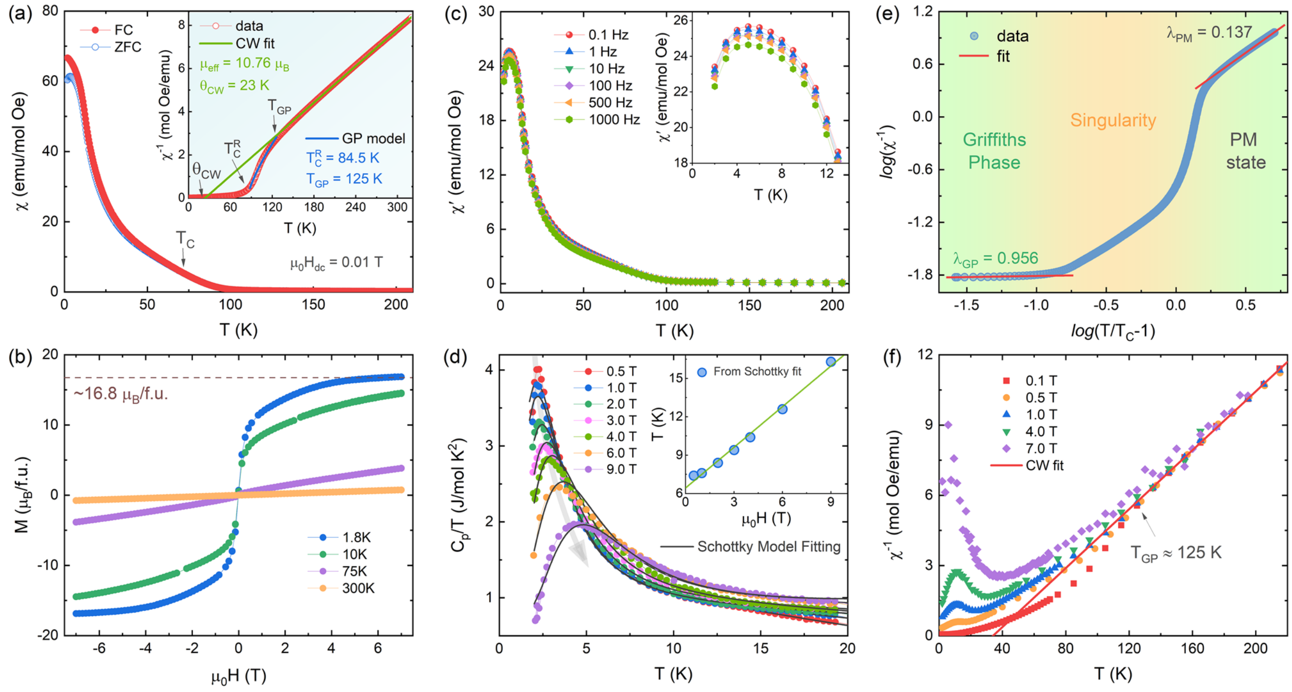

Fig. 6 | Analysis of magnetic and specific heat properties. **a** Temperature-dependent χ recorded in the ZFC/FC modes under $\mu_0H_{dc} = 0.01$ T. Inset shows the inverse susceptibility χ^{-1}(T) together with the CW and GP model fits. **b** Isothermal $M(\mu_0H)$ curves at different temperatures. **c** *ac* magnetic susceptibility (χ') frequency-dependent (0.1-1000 Hz). **d** Specific heat (C_p/T) curves together with Schottky Model fits at different μ_0H_{dc} (0.5–9.0 T), respectively. **e** $log\,\chi^{-1}$ vs $log\,T/(T_C-1)$ curve linearly fitted in both the FiM/FM and PM regimes with their respective λ values. **f** χ^{-1}(T) at different μ_0H_{dc} (0.1–7.0 T) and the CW fit (0.1 T curve) showing the GP suppressed.

presence of Cr *3d* peaks around −1.0 eV in the valence band and near 3.0 eV in the conduction band minimum suggests the possibility of *d*–*d* electronic transitions, consistent with a correlated insulating state.

Regarding the magnetic spin structure of Gd_2CrSbO_7, it is first necessary to note that magnetic interactions are primarily governed by long-range super-exchange pathways, especially those involving Cr^{3+}–O^{2-}–Gd^{3+}. Here, “long-range” refers to second-neighbor interactions and extended O-O-bridge super-exchange paths (e.g., Cr–O–O–Cr and Gd–O–O–B) rather than arbitrarily long distances across the lattice. Dominant super-exchanges include Cr–O–Cr and Gd–O–B pathways, with extended O–O bridges accounting for longer-range terms. Sb^{5+} behaves as a diamagnetic contribution and acts mainly as pathway dilution rather than a source of local magnetic moment. Consequently, the global exchange interactions promote FiM clusters between the Gd and Cr sublattices, as schematically illustrated by the FiM4 configuration in Fig. 7b, i.e., a configuration consistent with our experimental observation. Thus, based on our theoretical and experimental findings, we proposed a schematic illustration for the most probable short- and long-range exchange interactions that could be found in the Gd_2CrSbO_7 lattice, showing how these exchange interactions vary with temperature (see Fig. 7c). Herein, the magnetic interactions at the Cr/Sb sites are completely governed by the unpaired electrons in the Cr^{3+} ($3d^3$) ions, while Sb^{5+} ions remain magnetically inert due to its filled 4 *d* shell. Accordingly, we adopt only a collinear Heisenberg model on two sublattices (Cr and Gd), with first- and second-neighbor exchanges. To reflect B-site disorder (B = Cr/Sb), Gd–B couplings are treated as effective, configurationally averaged exchanges:

$$H = J_{nn}\sum_{\langle i,j\rangle\in Cr-Cr}\mathbf{S}_i\bullet\mathbf{S}_j + J_{nB}\sum_{\langle i,j\rangle\in Gd-B}\mathbf{S}_i\bullet\mathbf{S}_j + J'_{nn}\sum_{\langle\langle i,j\rangle\rangle\in Cr-Cr}\mathbf{S}_i\bullet\mathbf{S}_j + J'_{nB}\sum_{\langle\langle i,j\rangle\rangle\in Gd-B}\mathbf{S}_i\bullet\mathbf{S}_j, \qquad (4)$$

Here, $\langle i,j\rangle$ and $\langle\langle i,j\rangle\rangle$ denote first and second neighbors, respectively; $J > 0$ favors AFM (↑↓) coupling, while $J < 0$ favors FM (↑↑) coupling. The effective J_{nB} and J'_{nB} arise from configurational averaging over local B environments, making the model insensitive to the specific Cr/Sb arrangement. At low temperatures, $|J_{nn}|,|J'_{nn}| > |J_{nB}|,|J'_{nB}|$. However, with increasing temperature, $|J_{nn}|,|J'_{nn}|$ decrease and become comparable to $|J_{nB}|,|J'_{nB}|$, enhancing local FM/AFM competition and enabling spin flips at selected Gd sites (see Fig. 7c). This scenario leads locally to a competition between FM and AFM alignments, which could, in principle, generate magnetic frustrations through key super-exchange pathways, for instance, in Cr–O–Cr, Gd–O–Cr, and Gd–O–Gd. This condition certainly reduces the local FM character (i.e., $J_{nn}, J'_{nn} \approx J_{nB}, J'_{nB}$). Notably, B-site dilution by nonmagnetic Sb also reduces the connectivity of Cr-centered paths, which yields a reduced or frustrated long-range moment on the B-sublattice. The latter is represented in Fig. 7 by smaller B-site magnetic moments. Nevertheless, the system avoids a fully disordered state, because the oxygen spin polarization mediates the super-exchange and stabilizes a FiM-like alignment between the Gd and Cr sublattices, as supported by our experimental data. In other words, we did not find a fully magnetically frustrated state in our Gd_2CrSbO_7 compound, a feature that could point to a macroscopic non-collinear spin structure. Therefore, only collinear spin structures were calculated using the DFT method. In short, the excellent agreement between the calculated FiM4 ground state and our magnetic experimental data provides compelling evidence for this model, solidifying our understanding of Gd_2CrSbO_7 magnetic and electronic behavior.

Magnetocaloric performance

The MCE of the Gd_2CrSbO_7 pyrochlore was evaluated through the isothermal magnetic entropy change ($-\Delta S_M$), calculated from $M(\mu_0H, T)$ data at several temperatures (Supplementary Fig. 9). The methodology and equations used for these calculations are detailed in the Supplementary Section 6. The Arrott-plot (M^2 versus H/M), transformed from $M(\mu_0H)$ curves (Supplementary Fig. 10), revealed exclusively positive slopes,

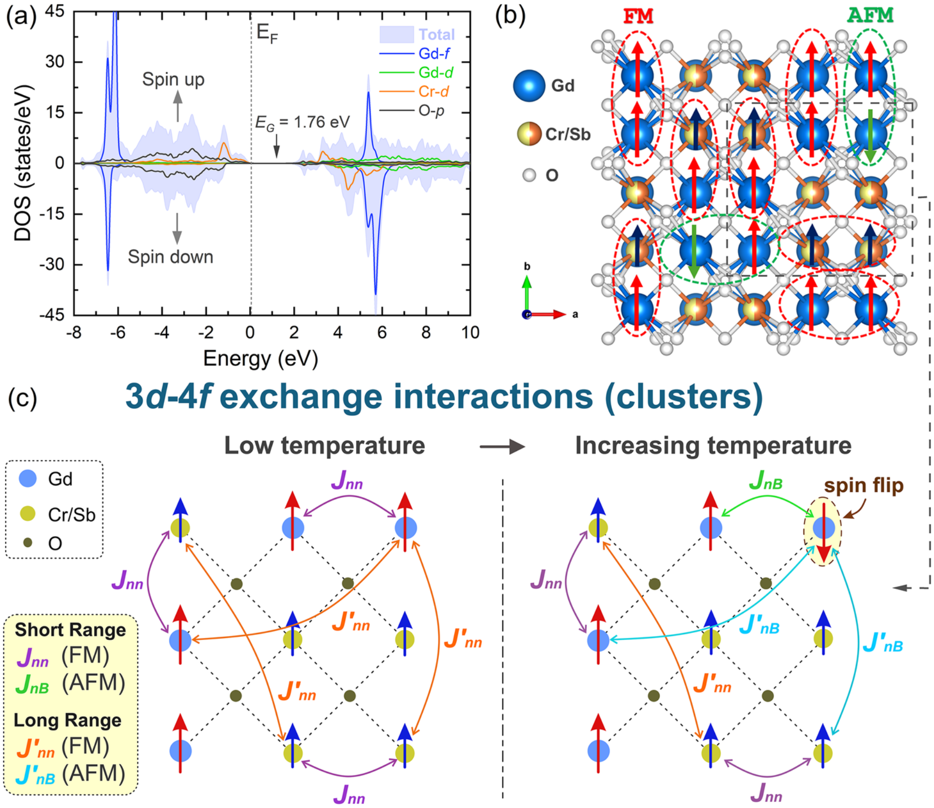

Fig. 7 | Spin-polarized DFT calculations and modeling of exchange interactions. **a** PBE + U total and projected spin-polarized density of states (TDOS and PDOS) calculated for dataset at 10 K in the ground state FiM alignment. The vertical dashed line indicates the Fermi energy level. **b** FiM spin configuration most likely at 10 K (FiM4) with both FM and AFM interactions possible. **c** Schematic illustration of the short- and long-range exchange interaction pathways between Cr-3*d* and Gd-4*f* (Cr–O–Cr, Gd–O–Cr, and Gd–O–Gd), representing also the Gd spin-flipping when there is a temperature increasing (**c**–right-hand side). B-site disorder is represented as Cr/Sb occupying the same Wyckoff site. Effective exchanges J_{nB} and J'_{nB} (Gd–B) are configurationally averaged, and therefore insensitive to the local Cr/Sb arrangement. Reduced long-range B-site moments are indicated by smaller arrows.

indicating a second-order phase transition (SOPT) in Gd_2CrSbO_7 across the investigated temperature and field ranges. The $-\Delta S_M(T)$ curves at different ΔB_{ap} of $0-1$ T ≤ ΔB_{ap} ≤ $0-7$ T are shown in Fig. 8a, where the data for the GGG[8] (at 0-2 T) are also included for comparison. The pronounced peak near 8 K with a maximum $-\Delta S_M$ ($-\Delta S_M{}^{max}$) reaching 4.7, 8.6, 13.5, 15.8, 18.3, 20.0, and 20.9 J/kg K for ΔB_{ap} of $0-1$, $0-2$, $0-3$, $0-4$, $0-5$, $0-6$, and $0-7$ T, respectively. As shown in the inset of Fig. 8a, the $-\Delta S_M^{max}$ follows the power law $-\Delta S_M^{max} \approx \left(\Delta B_{ap}\right)^m$ with the exponent $m = 0.67(2)$, corresponding to typical mean-field ferromagnets ($m = 2/3$)[50]. From the $-\Delta S_M(T)$ curves, we determined the order of magnetic phase transition by normalizing them under different applied field changes, constructed as $\Delta S_M/\Delta S_M^{max}(\theta)$ [51] (see detailed equations in Supplementary Section 6). The transformed $\Delta S_M/\Delta S_M^{max}(\theta)$ curves for a ΔB_{ap} of 0-1 up to 0-7 T are plotted in Fig. 8b. All the curves collapse onto a single master curve, a clear signature of a typical SOPT. Furthermore, the nature of the magnetic phase transition was confirmed by analyzing the exponent m (Fig. 8c), defined as $m(T,H) = d\left[\ln\left|\Delta S_M\right|\right]/d[\ln H]$. For $m < 2$, the transition is classified as SOPT, whereas $m > 2$ indicates a first-order phase transition (FOPT)[52]. As shown in Fig. 8c, the m(T) curves for Gd_2CrSbO_7 under various applied field changes ($\Delta(\mu_0 H)$) consistently yield values below 2, with no evidence of FOPT behavior ($m > 2$) within the tested temperature range, which further confirmed the SOPT nature of Gd_2CrSbO_7.

The refrigerating capacity (RC), a critical metric for evaluating the MCE of magnetocaloric materials, was estimated by:

$$\mathrm{RC} = \int_{T_1}^{T_2} \left|\Delta S_M\left(T, \mu_0 H\right)\right| dT \tag{5}$$

where, T_1 and T_2 are two temperatures corresponding to the cold side and the hot side, respectively[51]. The RC was calculated and is depicted in a contour plot temperature- and field-dependent in Fig. 8 d. It can be seen that RC reached a maximum of $RC^{max} = 430.2$ J/kg at 0–7 T (at temperature lower than 20 K). Moreover, RC^{max} increases nearly linearly with increasing magnetic field following $RC^{max} \approx (\Delta B_{ap})^p$ with $p = 1.16(7)$ (see Supplementary Fig. 11). This result indicates that the RC can be significantly enhanced by increasing the applied magnetic field. Notably, at a ΔB_{ap} of 0–5 T, the RC value of 274.3 J/kg surpasses those of other recently reported pyrochlores, such as $Gd_2Ti_2O_7$ (140.6 J/kg), $Tb_2Ti_2O_7$ (237.9 J/kg), and $Ho_2Ti_2O_7$ (244.1 J/kg)[53]. To further contextualize the performance of Gd_2CrSbO_7 compound, we extended the comparison to a range of magnetocaloric materials applicable in the cryogenic regime (T < 40 K). Figure 8e shows the ΔS_M performance of Gd_2CrSbO_7 compared to materials with pyrochlore-type structures and Gd-containing perovskites. A Table comparing the $|\Delta S_M|$, T_{MCE} and RC/RCP values of these materials can be found in Supplementary Table 6. As a result, the magnetocaloric performance of Gd_2CrSbO_7 (with $-\Delta S_M{}^{max} \approx 21$ J/kg·K at 0–7 T) is comparable to or exceeds the performance of other reported similar materials, such as $RE_2Mn_2O_7$ (RE = Er, Dy, Ho, and Yb)[22,23] and $RE_2Ti_2O_7$ (RE = Gd, Tb, and Ho)[53]. Quantitatively, the $\Delta S_M{}^{max}$ value of Gd_2CrSbO_7 was approximately 55% of the commercial magnetic refrigerant $Gd_3Ga_5O_{12}$ (GGG), with a $\Delta S_M{}^{max}$ reaches ~38 J/kg K under ΔB_{ap} of 0–7 T[54]. Therefore, the combination of significant refrigerating capacity and substantial magnetic entropy change results in remarkable magnetocaloric performance of Gd_2CrSbO_7, which makes it a promising candidate for cryogenic refrigeration as a solid refrigerant.

Concluding Remarks

Through a combination of experimental and computational techniques, we have systematically investigated the structural, electronic, magnetic, and magnetocaloric properties of the Gd_2CrSbO_7 pyrochlore. SXRD, PDF, and STEM analysis revealed that the material crystallizes in a single phase within the cubic $Fd\bar{3}m$ space group, characteristic of pyrochlore structures. The corner-sharing network of Cr/Sb octahedra and edge-sharing Gd polyhedral form a geometrically frustrated lattice, which directly influences the material magnetic behavior, which the additional Gd—O—Cr—O—Gd super-exchange interactions mediate AFM and FM coupling between $4f^7$-

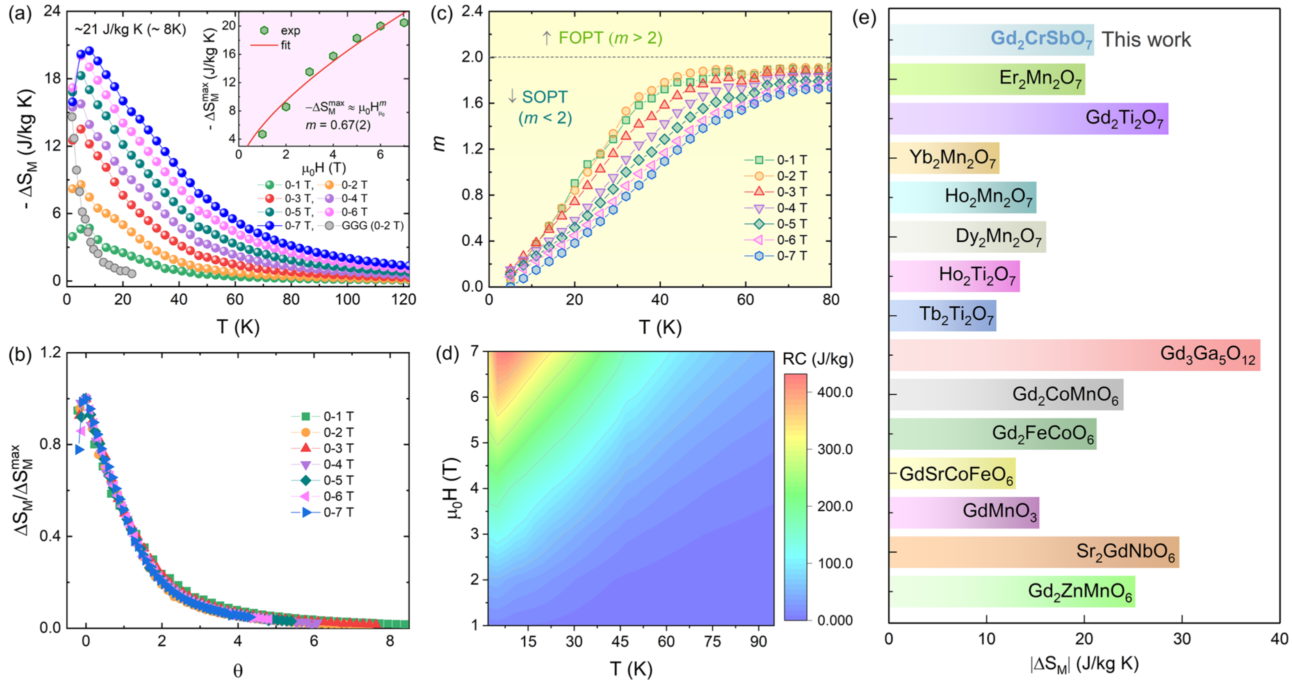

Fig. 8 | Magnetocaloric performance analysis and comparison with other materials. a $\Delta S_M(T)$ curves at different applied field changes $0-1\ T \leq \Delta(\mu_0 H) \leq 0-7\ T$. The data for GGG (at 0–2 T) was also included to comparison. Inset shows the $\Delta S_M^{max}(\mu_0 H)$ curve fitting following the power law $\Delta S_M^{max} \approx (\mu_0 H)^m$. **b, c** Universal $\Delta S_M/\Delta S_M^{max}(\theta)$ and exponent m curves, respectively. **d** Contour plot of temperature- and field-dependent refrigerating capacity RC for Gd_2CrSbO_7. **e** Comparing the $|\Delta S_M|$ performance of Gd_2CrSbO_7 with pyrochlore-type structure and Gd-containing perovskites in the cryogenic regime (T < 40 K).

Gd^{3+} and $3d^3$-Cr^{3+} ions, resulting in the FiM order. Temperature-dependent SXRD analysis of mean square displacements (U_{iso}) revealed structural stability at the Gd and Cr/Sb sites across the magnetic transition, while the O1 and O2 sites exhibited anomalous behavior between 25–225 K, suggesting a magnetoelastic effect that mediates the complex super-exchange interactions. Extended X-ray absorption fine structure (EXAFS) analysis further highlighted the covalent nature of the Sb–O bond, which influences the electronic environment of Cr and Gd ions. The weaker Sb–Gd interactions make the Gd and Cr sublattices more susceptible to magnetic fluctuations, contributing to the magnetic competition and the emergence of a Griffith-like phase. X-ray Raman data, particularly the Cr L_{23} spectrum, confirm the super-exchange interactions between Cr and O. Additionally, the experimental Gd N_{45} spectra are well reproduced by Gd^{3+} $(4f^7, 5d^0, 6s^0)$ configuration, further validating the local environment of Gd ions. DFT calculations corroborated these findings, revealing FiM coupling between Gd and Cr spins at low temperatures, driven by parallel alignment of most Gd spins with the FM Cr^{3+} sublattice. Increasing the temperature, Gd spins exhibit a tendency toward AFM coupling, reducing FM character and enhancing short-range interactions. The Griffiths-like phase and Schottky anomaly (observed below 10 K) arise from short-range Cr–Cr correlations and crystal field transitions of Gd *f*-electrons, respectively, both influenced by the local electronic environment. These magnetic interactions underpin the material significant magnetocaloric performance, characterized by a maximum magnetic entropy change of $-\Delta S_M{}^{max} \approx 21$ J/kg K and a relative cooling power of RC ≈ 430 J/Kg (at 0−7 T). These values surpass those of other recently reported pyrochlores and reach ~55% of performance of the commercial magnetic refrigerant $Gd_3Ga_5O_{12}$. We argue that the pronounced magnetic entropy change observed at low temperatures in Gd_2CrSbO_7 can be attributed to the remarkable thermal stability of its crystallographic structure below 60 K, as revealed by temperature-dependent SXRD analysis. The absence of significant variations in lattice parameters and unit cell volume indicates a suppression of lattice dynamics in this regime. This structural stabilization is critical for enhancing magnetocaloric performance, as it minimizes intrinsic heat dissipation caused by phonon vibrations and reduces spin-lattice coupling effects. Consequently, the refrigerant capacity is significantly improved in the cryogenic range (T < 40 K), where the decreased lattice vibrations and optimized Gd−Cr magnetic interactions lead to a more efficient magnetic entropy change. Associated, the significant cryogenic MCE in the Gd_2CrSbO_7 pyrochlore arises likely from the $4f$−$3d$ exchange interactions between the Gd and Cr sublattices, since most of them exhibit FM coupling at low temperatures. These features make Gd_2CrSbO_7 a viable material for low-temperature magnetic refrigeration, where minimizing energy losses is essential for achieving optimal cooling efficiency. By integrating multiple experimental techniques, this study provides a comprehensive understanding of the fundamental properties of Gd_2CrSbO_7 and demonstrates its potential as a promising candidate for cryogenic magnetic refrigeration applications. Lastly, the synergy of experimental methods underscores the importance of a multifaceted approach in studying complex materials, facilitating the rational design of new systems with tailored properties for advanced technological applications. Future investigations could explore the effects of chemical substitutions or external stimuli, such as pressure, to further optimize material performance and unveil new phenomena.

Methods

Sample synthesis

The Gd_2CrSbO_7 sample was synthesized by the modified sol-gel method. Appropriate amounts of $Gd(NO_3)_3{\cdot}6H_2O$, $Cr(NO_3)_3{\cdot}6H_2O$, and Sb_2O_3 with a 2:1:1 (Gd:Cr:Sb) ratio were dissolved in 5 mL of distilled water, followed by the addition of glycine ($C_2H_5NO_2$) as a chelating agent. Then, the homogenized solution was dried at 100 °C for 24 hours for gelification and dehydration. Afterward, the obtained xerogel was calcined at 1000 °C (4 h).

Synchrotron X-ray diffraction and Total scattering data collection

The Synchrotron X-ray diffraction (SXRD) and total scattering (TS) data were collected using the high-resolution powder diffractometer at beamline ID22 at the European Synchrotron Radiation Facility (ESRF)[55] (experiments MA-5866 and CH-6713). The SXRD patterns were collected at a wavelength of λ = 0.35429 Å (~35 keV) over the range 1−40° (2θ) in continuous scanning mode at 6-300 K range with a 5 min waiting time at each temperature step to guarantee an isothermal condition. For the room temperature total scattering experiment, the wavelength was calibrated to 0.206689(1) Å (60 keV) from refinement of PXRD data collected on a NIST standard LaB_6 660b standard. The sample was packed in a 0.3 mm borosilicate capillary and sealed using two-component epoxy glue. During measurement, the capillary was spun at 919 rpm and continuously rocked +/-1 mm to improve powder averaging. The scattering data were collected using the Perkin Elmer 2D detector (sum of 50 × 1 sec exposures) positioned at 380 mm behind the sample capillary, giving a Q_{max} of approx. 25 $Å^{-1}$. For the low temperature TS experiments (30 and 150 K), the measurements were performed using a high-resolution setup and the wavelength was calibrated to 0.427865(4) Å (29 keV) from refinement of PXRD data collected on a Si standard sample.

Rietveld analysis

Rietveld analysis of the SXRD and total scattering (TS) data was performed using the *FullProf Suite* software package[56]. The crystal structure Gd_2CrSbO_7 was refined based on the cubic pyrochlore structure (space group *Fd*-3*m*, no. 227)[57]. The atomic occupancies were kept fixed to match the nominal Gd_2CrSbO_7 composition, while atomic positions, scale factor, unit cell parameters, zero shift, and isotropic thermal parameter (B_{iso}) were refined. The background was described by a linear interpolation between a set of background points with refinable intensity. The peak profiles were modeled using the Thompson–Cox–Hastings formulation of the pseudo-Voigt function[58]. The instrumental contribution to the total peak broadening was determined by refinement of data collected on a NIST LaB_6 660b calibrant in the same instrumental configuration and deconvoluted from the sample broadening in the refinements. The remaining sample contribution to the peak broadening was attributed to microstrain (Stokes-Wilson).

PDF analysis of TS data analysis

The PDFs were obtained using the *PDFgetX3* software[59]. To allow isolation of the scattering from the sample itself for PDF analysis, the scattering pattern from an empty 0.3 mm borosilicate capillary in the same instrumental configuration was subtracted. The real-space structural refinements of the PDFs were carried out using the *PDFgui* software[60]. The experimental Q_{damp} (instrumental damping of the PDF peak intensities) was determined to be 0.009 $Å^{-1}$ by refinement of a NIST LaB_6 660b standard data collected in the same instrumental configuration.

Scanning Transmission Electron Microscopy (STEM)

The STEM and EELS (electron energy loss spectroscopy) measurements were performed using the JEOL ARM200cF operated at 200 keV, equipped with a Gatan Quantum EELS system and a spherical aberration corrector.

X-ray absorption spectroscopy

X-ray absorption spectroscopy (XAS) data were recorded at the BL22-CLÆSS station[61] of the ALBA Synchrotron (Barcelona, Spain) in transmission mode at the Sb *K*-edge (30.491 keV). In this experiment, a collimated and unfocused beam measuring of 0.3 × 1 mm^2 (V × H) was used. The monochromatic beam was delivered by a pair of LN_2-cooled Si(311) crystals. Finely ground powders were mixed with boron nitride (BN) and pelletized into 5 mm diameter disks to achieve an optimal absorption edge jump of ~0.35. Low-temperature measurements were conducted using an Norhof Liquid N_2 cryostream cooler in the temperature range 100−500 K. The absorption coefficient was determined by measuring the photon flux with ionization chambers placed before and after the sample. Extended X-ray absorption fine structure (EXAFS) spectra were collected over a *k*-range extending to 15 $Å^{-1}$. EXAFS oscillations, $\chi(k)$, were extracted using *Athena* software[62], which facilitated pre-edge background subtraction, edge jump normalization, and isolation of extended-range oscillations. Fourier transformation (FT) of the *k*-weighted $k^3\chi(k)$ oscillations was performed with a Hanning-type apodization function in both *k*- and *R*-spaces, using a *k*-range of 2–13 $Å^{-1}$ and an *R*-range of 1–4 Å. EXAFS fitting was conducted using *Artemis* software[62], employing theoretical single-scattering paths generated via FEFF multiple scattering path expansion, based on the Gd_2CrSbO_7 structure. These paths were refined against the experimental spectra by optimizing key EXAFS parameters, including path length (d), Debye–Waller factor (σ^2), and coordination number (N).

X-ray Raman scattering experiment

All X-ray Raman scattering (XRS) data were taken at beamline ID20 of the ESRF, Grenoble, France, using the large-solid-angle spectrometer[63]. Photons from three *U*26 undulators were monochromatized using a combination of a Si(111) high-heat-load pre- and a Si(311) channel-cut post-monochromator. X-rays were focused to a 20 × 20 μm^2 spot size at the sample position. We pressed the polycrystalline Gd_2CrSbO_7 samples into small pellets of 5 mm diameter and several 100 μm thickness. Inelastically scattered X-rays were analyzed using 48 spherically bent Si(660) analyzer crystals in Johann geometry, 12 at low momentum transfer (3.2 $Å^{-1}$), 12 at intermediate momentum transfer (6.4 $Å^{-1}$), and 24 at high momentum transfer (9.1 $Å^{-1}$). Energy loss spectra in the vicinity of the Cr $L_{2,3}$-, O *K*-, and Gd $N_{4,5}$-edges were obtained by varying the incident energy at a fixed analyzer energy of 9.68 keV. The overall energy resolution was 0.7 eV. For each of the three excitation edges, several scans were taken, checked for consistency, and averaged over. All data treatment was performed with the IXStools program package as described elsewhere[64]. The total scanning time was 12 h. Simulations of the O *K*-edge were performed using the *FDMNES* program package[65] including the momentum transfer dependence[44]. We used the Hilbert++ full charge transfer multiplet code for the calculation of the Cr $L_{2,3}$- and Gd $N_{4,5}$-edges[38,39].

Magnetic and transport properties

The magnetic properties were measured with a SQUID magnetometer (MPMS-3), from Quantum Design (San Diego, USA) in a temperature range from 1.8 up to 300 K and a range of magnetic fields up to 7 T. The *ac* susceptibility was measured in a PPMS Quantum Design (San Diego, USA) with the *ac* susceptometer in a frequency range from 100 Hz up to 10 kHz, with an oscillatory field with an amplitude of 1 Oe. The samples were also measured in different external magnetic fields of $H = 0.0$, 0.05, 0.5, and 1.5 T under a fixed frequency of 10 Hz. The heat capacity was also measured in the PPMS with an adiabatic heat pulse method. For this, the ceramic pellets were cut with a diamond saw to fit into the sample-holder dimensions.

Computational details

The electronic structure and magnetic characteristics of Gd_2CrSbO_7 system were investigated using first-principles DFT calculations[66,67], based on the full-potential linearized augmented-plane-wave (FP-LAPW) method[68], implemented via the *WIEN2K* software package[69]. The exchange-correlation effects were treated with the PBEsol functional[70], combined with an effective Hubbard potential $U_{eff} = U - J$, following the scheme proposed by Anisimov et al.[71]. To accurately describe the highly localized *f*-electrons of Gd and *d*-states of Cr, we applied 7.0 eV for Gd and 4.2 eV for Cr ions. The radii R_{MT} of the muffin-tin spheres were set to 2.00, 1.85, 1.95, and 1.54 a.u. for Gd, Cr, Sb, and O, respectively. Atomic-like functions within these spheres were expanded up to $l_{max} = 10$, and the interstitial region was represented by a plane-wave expansion truncated at $k_{max} = 6.0/R_{MT(O)}$. The charge density was Fourier-expanded with $G_{max} = 16$, while the valence electron states of O ($2s^2 2p^4$), Sb ($4d^{10} 5s^2 5p^3$), Cr ($3d^5 4s^1$), and Gd ($4f^7 5d^1 6s^2$) were explicitly treated in the calculations. For the *k*-space integration, we employed a 5×5×5 Monkhorst-Pack grid in the irreducible part of the Brillouin zone. Relaxation of internal parameters was carried out until the interatomic forces were reduced to less than 2 mRy/bohr. In the self-consistent calculations, the convergence was achieved with an energy threshold of 10^{-5} Ry and a charge transfer criterion of 10^{-5} $e/bohr^3$. To model B-site disorder, we considered a set of representative random Cr/Sb configurations within a supercell and verified that the total energies and local magnetic moments show only minor variations across configurations. The effective couplings employed in the model correspond to configurational averages over these realizations.

Data availability

All data generated or analysed during this study are included in this published article (and its supplementary information files). Additional experimental and calculation data are available from the corresponding authors via email (ja.alonso@icmm.csic.es and/or rsantoss@ucm.es) upon reasonable request.

Received: 21 April 2025; Accepted: 19 November 2025;

References

1. Zhang, Y., Na, Y., Hao, W., Gottschall, T. & Li, L. Enhanced Cryogenic Magnetocaloric Effect from 4f-3d Exchange Interaction in B-Site Ordered Gd_2CuTiO_6 Double Perovskite Oxide. *Adv. Funct. Mater.* **34**, 2409061 (2024).
2. Franco, V. et al. Magnetocaloric effect: From materials research to refrigeration devices. *Prog. Mater. Sci.* **93**, 112–232 (2018).
3. Zhang, F., Miao, X., van Dijk, N., Brück, E. & Ren, Y. Advanced Magnetocaloric Materials for Energy Conversion: Recent Progress, Opportunities, and Perspective. *Adv. Energy Mater*. **14**, 2400369 (2024).
4. Yang, Z. W. et al. Exceptional Magnetocaloric Responses in a Gadolinium Silicate with Strongly Correlated Spin Disorder for Sub-Kelvin Magnetic Cooling. *Adv. Sci.* **11**, e2306842 (2024).
5. Barclay, J. A. & Steyert, W. A. Materials for magnetic refrigeration between 2 K and 20 K. *Cryogenics*. **22**, 73–80 (1982).
6. Mukherjee, P. & Dutton, S. E. Enhanced Magnetocaloric Effect from Cr Substitution in Ising Lanthanide Gallium Garnets $Ln_3CrGa_4O_{12}$ (Ln = Tb, Dy, Ho). *Adv. Funct. Mater*. **27**, 1701950 (2017).
7. Delacotte, C. et al. $NaGdS_2$: A promising sulfide for cryogenic magnetic cooling. *Chem. Mater*. **34**, 1829–1837 (2022).
8. Liu, P. et al. Ultralow-field magnetocaloric materials for compact magnetic refrigeration. *NPG Asia Mater*. **15**, 41 (2023).
9. Chen, Y. C. et al. A brilliant cryogenic magnetic coolant: Magnetic and magnetocaloric study of ferromagnetically coupled GdF_3. *J. Mater. Chem. C* **3**, 12206–12211 (2015).
10. Tziotzi, T. G. et al. A $\{Gd_{12}Na_6\}$ molecular quadruple-wheel with a record magnetocaloric effect at low magnetic fields and temperatures. *J. Am. Chem. Soc.* **145**, 7743–7747 (2023).
11. Vasile, R. L. et al. Magnetocaloric properties in rare-earth-based metal-organic frameworks: influence of magnetic density and hydrostatic pressure. *Inorg. Chem.* **62**, 19741–19748 (2023).
12. Palacios, E. et al. Magnetic structure and magnetocalorics of $GdPO_4$. *Phys. Rev. B - Condens. Matter Mater. Phys*. **90**, 214423 (2014).
13. Yang, Z. W. et al. Strong Magnetocaloric Coupling in Oxyorthosilicate with Dense Gd^{3+} Spins. *Inorg. Chem.* **62**, 5282–5291 (2023).
14. Lorusso, G. et al. A dense metal-organic framework for enhanced magnetic refrigeration. *Adv. Mater.* **25**, 4653–4656 (2013).
15. Chen, Y. C. et al. Study of a magnetic-cooling material $Gd(OH)CO_3$. *J. Mater. Chem. A* **2**, 9851–9858 (2014).
16. Xu, Q. et al. $Gd(OH)F_2$: a promising cryogenic magnetic refrigerant. *J. Am. Chem. Soc.* **144**, 13787–13793 (2022).
17. Silva, R. S. et al. Magnetoelastic coupling and cryogenic magnetocaloric effect in two-site disordered $GdSrCoFeO_6$ double perovskite. *Chem. Mater.* **35**, 2439–2455 (2023).
18. Koskelo, E. A. C., Liu, C., Mukherjee, P., Kelly, N. D. & Dutton, S. E. Free-spin dominated magnetocaloric effect in dense Gd^{3+} double perovskites. *Chem. Mater.* **34**, 3440–3450 (2022).
19. Gardner, J. S., Gingras, M. J. P. & Greedan, J. E. Magnetic pyrochlore oxides. *Rev. Mod. Phys.* **82**, 53–107 (2010).
20. Bramwell, S. T. & Gingras, M. J. P. Spin ice state in frustrated magnetic pyrochlore materials. *Science* **294**, 1495–1501 (2001).
21. Zhang, Y., Hao, W., Lin, J., Li, H. F. & Li, L. Geometrically frustrated $Gd_2Ti_2O_7$ oxide: A comprehensive exploration of structural, magnetic, and magnetocaloric properties for cryogenic magnetic cooling applications. *Acta Mater*. **272**, 119946 (2024).
22. Cui, Q. et al. Large reversible magnetocaloric effect in the ferromagnetic pyrochlores $R_2Mn_2O_7$ (R = Dy, Ho, Yb). *J. Magn. Magn. Mater*. **490**, 165494 (2019).
23. Cai, Y. Q. et al. Giant reversible magnetocaloric effect in the pyrochlore $Er_2Mn_2O_7$ due to a cooperative two-sublattice ferromagnetic order. *Phys. Rev. Mater*. **1**, 064408 (2017).
24. Wang, L., Ouyang, Z., Li, Z., Cao, J. & Xia, Z. Large magnetocaloric effect in $Gd_2Si_2O_7$ and plateau-like magnetic entropy change in $Dy_2Si_2O_7$. *J. Alloys Compd*. **969**, 172402 (2023).
25. Dwivedi, V. K., Mandal, P. & Mukhopadhyay, S. Frustration-Induced Inversion of the Magnetocaloric Effect and Metamagnetic Transition in Substituted Pyrochlore Iridates. *ACS Appl. Electron. Mater*. **4**, 1611–1618 (2022).
26. Koskelo, E. C. et al. Comparative study of magnetocaloric properties for Gd^{3+} compounds with different frustrated lattice geometries. *PRX Energy* **2**, 033005 (2023).
27. Nandi, S. et al. Magnetization process and specific heat properties of geometrically frustrated pyrochlores R_2FeSbO_7 (R^{3+} = Dy, Y) and spin-ice magnetic phase in Dy_2FeSbO_7. *J. Alloys Compd*. **714**, 318–330 (2017).
28. Whitaker, M. J. & Greaves, C. Magnetic ordering in the pyrochlore Ho_2CrSbO_7 determined from neutron diffraction, and the magnetic properties of other RE_2CrSbO_7 phases (RE = Y, Tb, Dy, Er). *J. Solid State Chem*. **215**, 171–175 (2014).
29. Nandi, S. et al. Magnetothermodynamic properties of frustrated pyrochlore Gd_2FeSbO_7 in cooperative two-sublattice molecular-field model. *J. Magn. Magn. Mater*. **500**, 166381 (2020).
30. Zhao, H. et al. Antiferroelectricity-Induced Negative Thermal Expansion in Double Perovskite Pb_2CoMoO_6. *Small* **20**, 2305219 (2023).
31. Vočadlo, L., Knight, K. S., Price, G. D. & Wood, I. G. Thermal expansion and crystal structure of FeSi between 4 and 1173 K determined by time-of-flight neutron powder diffraction. *Phys. Chem. Miner.* **29**, 132–139 (2002).
32. Ruff, J. P. C. et al. Structural fluctuations in the spin-liquid state of $Tb_2Ti_2O_7$. *Phys. Rev. Lett*. **99**, 237202 (2007).
33. Nakatsuka, A., Yoshiasa, A., Fujiwara, K. & Ohtaka, O. Variable-temperature single-crystal X-ray diffraction study of $SrGeO_3$ high-pressure perovskite phase. *J. Mineral. Petrol. Sci.* **113**, 280–285 (2018).
34. Rodrigues, J. E. F. S. et al. Experimental and theoretical investigations on the structural, electronic, and vibrational properties of $Cs_2AgSbCl_6$ double perovskite. *Ind. Eng. Chem. Res.* **60**, 18918–18928 (2021).
35. Fornasini, P. Study of lattice dynamics via extended X-ray absorption fine structure. *J. Phys. Condens. Matter* **13**, 7859 (2001).
36. Rodrigues, J. E. F. S. et al. Atomic structure and lattice dynamics of $CoSb_3$ Skutterudite-based thermoelectrics. *Chem. Mater.* **34**, 1213–1224 (2022).
37. Willis, B. T. M. & Pryor, A. W. *Thermal Vibrations in Crystallography*. (Cambridge University Press, 1975).
38. Mirone, A., Sacchi, M. & Gota, S. Ligand-field atomic-multiplet calculations for arbitrary symmetry. *Phys. Rev. B - Condens. Matter Mater. Phys*. **61**, 13540 (2000).
39. Longo, A. et al. An Original Empirical Method for Simulating V $L_{2,3}$ Edges: The Example of $KVPO_4F$ and $KVOPO_4$ Cathode Materials. *J. Phys. Chem. C* **126**, 19782–19791 (2022).
40. Gordon, R. A. et al. High multipole transitions in NIXS: Valence and hybridization in 4 f systems. *EPL* **81**, 26004 (2008).
41. Sahle, C. H. J. et al. The Ba 4d-4f giant dipole resonance in complex Ba/Si compounds. *J. Phys. B At. Mol. Opt. Phys*. **47**, 045102 (2014).
42. Longo, A. et al. Oxygen vacancy clusters in bulk cerium oxide and the impact of gold atoms. *Cell Rep. Phys. Sci*. **4**, 101699 (2023).

43. Mirone, A., Rovezzi, M., Sahle, C. & Longo, A. Beyond the Bethe-Salpeter equation in DFT based computational spectroscopy. arXiv https://doi.org/10.48550/arXiv.2502.04690 (2025).
44. Joly, Y., Cavallari, C., Guda, S. A. & Sahle, C. J. Full-Potential Simulation of X-ray Raman Scattering Spectroscopy. *J. Chem. Theory Comput.* **13**, 2172–2177 (2017).
45. Li, X. et al. Long-range magnetic order in the Heisenberg pyrochlore antiferromagnets $Gd_2Ge_2O_7$ and $Gd_2Pt_2O_7$ synthesized under high pressure. *Phys. Rev. B* **94**, 214429 (2016).
46. Bonville, P. et al. Low temperature magnetic properties of geometrically frustrated $Gd_2Sn_2O_7$ and $Gd_2Ti_2O_7$. *J. Phys. Condens. Matter* **15**, 7777 (2003).
47. Wang, Y. et al. Giant Low-Field Cryogenic Magnetocaloric Effect in a Polycrystalline EuB_4O_7 Compound. *J. Am. Chem. Soc*. **146**, 3315–3322 (2024).
48. Silva, R. S. et al. Griffiths-like phase, large magnetocaloric effect, and unconventional critical behavior in the $NdSrCoFeO_6$ disordered double perovskite. *Phys. Rev. B* **106**, 1–21 (2022).
49. Sibille, R. et al. Candidate Quantum Spin Liquid in the Ce^{3+} Pyrochlore Stannate $Ce_2Sn_2O_7$. *Phys. Rev. Lett*. **115**, 097202 (2015).
50. Sahoo, R. C., Das, S. & Nath, T. K. Role of Gd spin ordering on magnetocaloric effect and ferromagnetism in Sr substituted Gd_2CoMnO_6 double perovskite. *J. Appl. Phys*. **124**, 103901 (2018).
51. Xie, H. et al. A brilliant magnetic refrigerant operating near liquid helium temperature: enhanced magnetocaloric effect in ferromagnetic $EuTi_{0.75}Al_{0.125}Zr_{0.125}O_3$. *Adv. Electron. Mater.* **10**, 2400176 (2024).
52. Law, J. Y. et al. A quantitative criterion for determining the order of magnetic phase transitions using the magnetocaloric effect. *Nat. Commun.* **9**, 2680 (2018).
53. Xu, B. et al. Magnetic properties and cryogenic magnetocaloric effect of pyrochlore structure $RE_2Ti_2O_7$ (RE = Gd, Tb, and Ho) compounds. *J. Appl. Phys*. **135**, 075104 (2024).
54. Sackville Hamilton, A. C., Lampronti, G. I., Rowley, S. E. & Dutton, S. E. Enhancement of the magnetocaloric effect driven by changes in the crystal structure of Al-doped GGG, $Gd_3Ga_{5-x}Al_xO_{12}$ ($0 \le x \le 5$). *J. Phys. Condens. Matter* **26**, 116001 (2014).
55. Fitch, A. et al. ID22 – the high-resolution powder-diffraction beamline at ESRF. *J. Synchrotron. Radiat.* **30**, 1003–1012 (2023).
56. Rodríguez-Carvajal, J. Recent advances in magnetic structure determination by neutron powder diffraction. *Phys. B Phys. Condens. Matter* **192**, 55–69 (1993).
57. Casado, P. G., Mendiola, A. & Rasines, I. Preparation and crystallographic data of the pyrochlores Gd_2MSbO_7 (M = Cr, Mn, Fe, In). *J. Phys. Chem. Solids* **46**, 921–923 (1985).
58. Thompson, P., Cox, D. E. & Hastings, J. B. Rietveld refinement of Debye–Scherrer synchrotron X-ray data from Al_2O_3. *J. Appl. Crystallogr.* **20**, 79–83 (1987).
59. Juhás, P., Davis, T., Farrow, C. L. & Billinge, S. J. L. PDFgetX3: A rapid and highly automatable program for processing powder diffraction data into total scattering pair distribution functions. *J. Appl. Crystallogr*. **46**, 560–566 (2013).
60. Farrow, C. L. et al. PDFfit2 and PDFgui: Computer programs for studying nanostructure in crystals. *J. Phys. Condens. Matter* **19**, 335219 (2007).
61. Simonelli, L. et al. CLAESS: The hard X-ray absorption beamline of the ALBA CELLS synchrotron. *Cogent Phys.* **3**, 1–10 (2016).
62. Ravel, B. & Newville, M. ATHENA and ARTEMIS. in 1–5 (Wiley Online Library, 2020). https://doi.org/10.1107/S1574870720003353.
63. Huotari, S. et al. A large-solid-angle X-ray Raman scattering spectrometer at ID20 of the European Synchrotron Radiation Facility. *J. Synchrotron. Radiat*. **24**, 521–530 (2017).
64. Sahle, C. J. et al. Planning, performing and analyzing X-ray Raman scattering experiments. in *J. Synchrotron. Radiat*. **22**, 400–409 (2015).
65. Joly, Y. X-ray absorption near-edge structure calculations beyond the muffin-tin approximation. *Phys. Rev. B - Condens. Matter Mater. Phys*. **63**, 125120 (2001).
66. Hohenberg, P. & Kohn, W. Inhomogeneous electron gas. *Phys. Rev*. **136**, B864 (1964).
67. Kohn, W. & Sham, L. J. Self-consistent equations including exchange and correlation effects. *Phys. Rev*. **140**, A1133 (1965).
68. Andersen, O. K. Linear methods in band theory. *Phys. Rev. B* **12**, 3060 (1975).
69. Blaha, P., Schwarz, K., Madsen, G., Kvasnicka, D. & Luitz, J. *WIEN2k: An Augmented Plan Wave Plus Local Orbitals Program for Calculating Crystal Properties*. *Institute of Physical and Theoretical Chemistry, TU Vienna* vol. 2 (2014).
70. Perdew, J. P. et al. Restoring the density-gradient expansion for exchange in solids and surfaces. *Phys. Rev. Lett.* **100**, 136406 (2008).
71. Anisimov, V. I., Poteryaev, A. I., Korotin, M. A., Anokhin, A. O. & Kotliar, G. First-principles calculations of the electronic structure and spectra of strongly correlated systems: Dynamical mean-field theory. *J. Phys. Condens. Matter* **9**, 7359 (1997).
72. Momma, K. & Izumi, F. VESTA 3 for three-dimensional visualization of crystal, volumetric and morphology data. *J. Appl. Crystallogr*. **44**, 1272–1276 (2011).

Acknowledgements

We would like to express our gratitude to the Spanish Ministry for Science and Innovation (MCIN/AEI/10.13039/501100011033) for their financial support of the following projects: PID2021-122477OB-I00, PID2021-122980OB-C51, TED2021-129254B-C21, and TED2021-129254B−C22. This project has received funding from Conselho Nacional de Desenvolvimento Científico e Tecnológico-CNPq (grant nos. 309184/2022-3, 403722/2021-7, and 310167/2021-3), Fundação de Amparo à Pesquisa e Inovação do Espírito Santo (FAPES-Brazil: TO-640/2022), and the European Union's Horizon Europe research and innovation programme under project No 101063369 (OXYPOW). The electron microscopy and spectroscopy were performed in the National Centre for Electron Microscopy in Madrid, in the framework of ICTS-ELECMI. XAS experiment (proposals 2024028300 and 2023097812) was performed at CLÆSS beamline at ALBA Synchrotron with the collaboration of ALBA staff. We are grateful to the ESRF for making their facilities available for the necessary experiments MA-5866 (10.15151/ESRF-ES-1304132154) and CH-6713 (10.15151/ESRF-ES-1453488999).

Author contributions

Crystallographic parameters from TS and SXRD; volumetric thermal variation; local structure from EXAFS; derivative and frequency- and field-dependent magnetization; DFT calculations for different Gd and Cr spin configurations; MCE analysis; RC^{max} field-dependent.

Competing interests

The authors declare no competing interests.

Additional information

Supplementary information The online version contains supplementary material available at https://doi.org/10.1038/s43246-025-01024-6.

Correspondence and requests for materials should be addressed to R. S. Silva Jr or J. A. Alonso.

Peer review information *Communications Materials* thanks the anonymous reviewers for their contribution to the peer review of this work.